METAL OXIDE AND 2D MATERIAL ELECTRODES FOR NEXT-GENERATION SUPERCAPACITOR: ZNO AND MXENE

by

AMEEN UDDIN AMMAR

Submitted to the Graduate School of Engineering and Natural Science in partial fulfillment of the requirements for the degree of Doctor of Philosophy

Sabanci University

December 2022

METAL OXİDE AND 2D MATERİAL ELECTRODES FOR NEXT-GENERATİON SUPERCAPACİTOR: ZNO AND MXENE

APPROVED BY:

Assoc. Prof. Dr. Emre Erdem (Thesis Supervisor)

Assoc. Prof. Dr. Burcu Saner Okan

Prof. Dr. Mustafa Tuncer

Prof. Dr. Nurdan Demirci Sankır

Asst. Prof. Dr. Yaşar Özkan Yeşilbağ

DATE OF APPROVAL: 28/12/2022

ABSTRACT

METAL OXIDE AND 2D MATERIAL ELECTRODES FOR NEXT-GENERATION
SUPERCAPACITOR: ZNO AND MXENE

AMEEN UDDIN AMMAR

Materials Science and Nanoengineering, Ph.D. Dissertation, December 2022

Dissertation supervisor: Assoc. Prof. Dr. Emre Erdem

Keywords: Supercapacitors, Zinc oxide, MXenes, Electron paramagnetic spectroscopy,
photoluminescence spectroscopy, Electrochemical Analysis.

Supercapacitors are gaining tremendous attention as energy storage devices for the benefits these devices can offer, like fast charge-discharge, high shelf life, and improved cyclic stability compared to other energy storage devices. Here in, we report the development of high-performance supercapacitor devices by using manganese-doped Zinc oxide nanowires (Mn-ZnO NWs), copper-doped zinc oxide nanoparticles (Cu-ZnO NPs), and cobalt doped Zinc Oxide nanoparticles (Co-ZnONPs)) as one electrode and MXene as the second electrode material. The synthesis of all the electrode materials is presented along with the structural, electronic, optical, and electrochemical analyses. Transitional metal doped ZnO (TM-ZnO) possess competing effect of intrinsic and extrinsic defect signals, which were analyzed by Electron paramagnetic resonance spectroscopy (EPR) and photoluminescence spectroscopy (PL), the presence of these defects increases the overall synergy between the components of supercapacitor device which leads to enhanced performance of our supercapacitor. TM-ZnO samples when used in combination with MXene as a second electrode, increased the performance of supercapacitors even further as MXene offered high conductivity and high surface area. The electrochemical result of the assembled supercapacitor when measured by techniques like cyclic voltammetry, impedance spectroscopy, and galvanostatic charge-discharge showed some encouraging results. The highest performance value for a supercapacitor was obtained to be 151 F/g specific capacitance with 84 Wh/kg energy density and a power density of 75 kW/kg.

ÖZET

YENİ NESİL SÜPERKAPASITOR İÇİN METAL OKSİT VE 2-BOYUTLU MALZEME ELEKTROTLARI: ÇİNKO OKSİT VE MXENE

AMEEN UDDIN AMMAR

Malzeme Bilimi ve Nanomühendislik, Doktora Tezi, Aralık 2022
Tez Danışmanı: Doç. Dr. Emre Erdem

Anahtar kelimeler: Süperkapasitör, Çinko oksit, MXene, Elektron Paramanyetik Spektroskopisi, Fotolüminisans Spektroskopisi, Elektrokimyasal Analiz.

Süperkapasitörler sahip oldukları hızlı şarj-deşarj, uzun raf ömrü ve gelişmiş döngüsel stabilite gibi sahip olduğu avantajlardan dolayı diğer enerji depolama cihazlarına oranla fazlaca ilgi görmektedir. Bu tezde mangan katkılı çinko oksit nanotel, bakır katkılı çinko oksit nanoparçacıklar ve kobalt katkılı nanoparçacıklar birincil elektrot malzemesi olarak, MXene de ikincil elektrot malzemesi olarak yüksek performanslı süperkapasitör cihazı geliştirilmesinde kullanılmıştır. Kullanılan elektrot malzemelerinin sentezleri; yapısal, elektronik, optik ve elektrokimyasal analiz yöntemleri ile karakterize edilmiştir. Geçiş metal katkılı çinko oksitler yapılarında kendinden sahip oldukları ve sonradan dış kaynaklı oluşan yapısal kusurlara sahiptir ve bu hatalar elektron paramanyetik rezonans spektroskopisi (EPR) ve fotolüminisans spektroskopi ile analiz edilmiştir. Bahsi geçen yapısal kusurların varlığının süperkapasitör bilesenleri arasındaki sinerjik etkileşimi arttırdığı ve elde edilen süperkapasitörün performansını geliştirdiği gözlemlenmiştir. MXene malzemelerinin sahip olduğu yüksek iletkenlik ve geniş yüzey alanı, MXene malzemelerinin ikinci elektrot olarak geçiş metal katkılı çinko oksit ile karşılıklı kullanılması, süperkapasitörün performansını ileri seviyede arttırmıştır. Üretilen süperkapasitörün elektrokimyasal özellikleri döngüsel voltametre, empedans spektroskopisi ve galvanostatik şarj-deşarj yöntemleri ile ölçüldüğünde kayda değer sonuçlar elde edilmiştir. Spesifik kapasitans değeri olarak 151 F/g, enerji yoğunluğu olarak 84 Wh/kg ve güç yoğunluğu olarak 75 kW/kg oldukça yüksek değerler olarak ölçülmüştür.

Acknowledgments

I would firstly like to thank Sabanci University for making me a part of this exceptional and amazing community. I am grateful to all the support and experience this institution has provided me, the facility Sabanci university provides to its students is the truly the best a person can ask for. This journey enabled me to push myself to my very limit and be the best the version of myself to have the ability to make a humble contribution befitting to this blessing.

First of all, I would like to thank and appreciate my supervisor Assoc. Prof. Dr. Emre Erdem for his unlimited support and kindness. He was extremely helpful, understanding, and considerate all the time. His belief in me and kept pushing me to come out of my comfort zone is the major reason that I am able to complete this work.

My thesis progress jury includes Assoc. Prof. Dr. Burcu Saner Okan and Prof. Dr. Mustafa Tuncer to make time for me to attend my progress meetings and guide me in the best possible way. It really helped me a lot.

My special mentions to Assoc. Prof. Feray Bakan-Misirlioglu from (SUNUM), Dr. Fatma Nur Tuzluca Yesilbag, Dr. Yasar Ozkan Yesilbag from Erzincan Binali Yıldırım University, and Prof. Dr. Salvo Mirabella, Dr. Giorgia Franzo, Prof. Dr. Guglielmo Guido Condorelli from Università di Catania, Italy for their fruitful collaboration in my research.

My lab colleagues deserve special thanks, they are the best team to work with. My lab partners include Mohammed Hasan Aleinawi, Ipek Deniz Yildirim, Dr. Merve Buldu-Akturk and Sumaiyah Najib. These are the most helping and highly efficient people I can possibly work with.

I am extremely grateful to my family that includes my mother, father brother, and sister for their support throughout this journey. Special mentions to my wife for all the comfort she provided me so I can focus on my work.

Contents

Table of Figures

List of Table

1. INTRODUCTION

Energy storage systems are considered to be the backbone if the renewable energy dream is to succeed. As most renewable sources are intermittent (are not available all the time) so storing the excess energy and using it when the source is not available is the only way forward in this regard. Energy storage systems then become important to achieve these results. There are different types of energy storage devices, some important are shown in Fig.1. The supercapacitor also known as the ultracapacitor or electrochemical capacitor, has gained a tremendous amount of attention in recent years. This attention is due to the relatively high power density, and long cycling life that supercapacitor offers compared to other energy storage devices [1]. The supercapacitor mechanism of storing charges is like a conventional capacitor but the charge does not accumulate in two conductors but the interface between the surface of a conductor and an electrolytic solution. The primary supercapacitor feature that makes it suitable for use in energy storage systems is the possibility of fast charge and discharge without loss of efficiency availability of numerous numbers of cycles [2].

Figure 1: Various types of energy storage devices [3].

Supercapacitors successfully bridge the gap between batteries that are high energy density devices but are typically low-power devices whereas conventional capacitors may have a power density of $> 10^6$ W/dm^3 at very low energy density, this phenomenon is shown in Fig. 2. Thus, supercapacitors

may improve battery performance in terms of power density or may improve capacitor performance in terms of energy density when combined with the respective device. Apart from their higher power capability, some additional features of supercapacitors are their long shelf and durability. Supercapacitors if unused self-discharge on low voltage over a period but can retain their capacitance and thus can be recharged to their original condition. Unlike most batteries which will degrade considerably and become useless if not used.
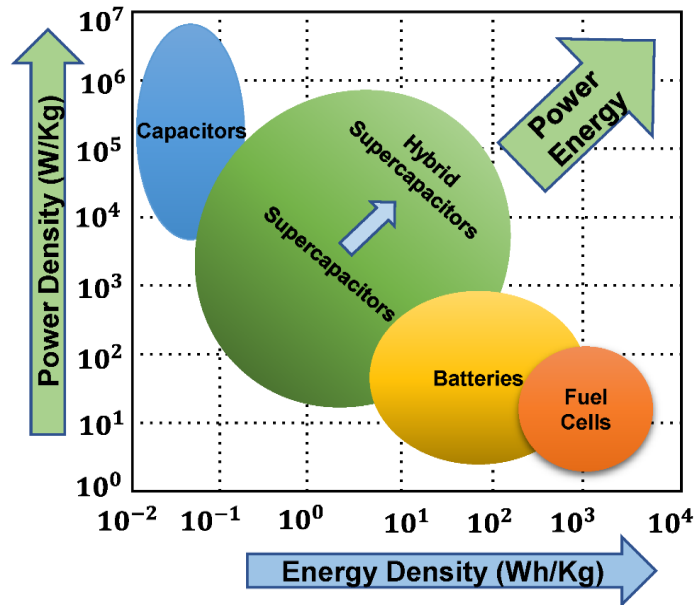
Figure 2: Ragone plot for energy storage devices [4].

Supercapacitors based on their charge storage mechanism can be divided into two main types, electrochemical double-layer capacitors (EDLC) and pseudo-capacitor. EDLC stores energy using an electric double layer created at the electrode/electrolyte interface. Charges accumulated at the electrode are by electrostatic mechanism and a non-faradic process takes place.

On the other hand, pseudo-capacitors store energy using faradaic reactions on the electrode material in this case, the electrons generated by the redox reaction are traveling across the interface of the electrode/electrolyte. This faradic process is the main reason for pseudo-capacitors having higher energy density than EDLC [5].

The energy density (E) of a supercapacitor can be calculated as.

$$E = \frac{CV^2}{2} \qquad\qquad (1)$$

where *C* shows the capacitance and *V* is the voltage.

The power density of a supercapacitor is measured as:

$$P = \frac{V^2}{4R} \qquad\qquad (2)$$

where *V* is the voltage and *R* is the resistance.

In addition, to the two above types, a third type where both EDLC and pseudo-capacitance mechanisms are simultaneously used is called the hybrid supercapacitor (HSC). By using both faradic and non-faradic reactions to store charges HSC possesses higher energy and power density with impressive cycling stability as well. A summary of the supercapacitor types and their performances is shown in Table 1.

Table 1: Types of Supercapacitors [6]

Supercapacitor Type	Electrode Material	Mechanism (Charge Storage)	Advantages	Limitation
Electrochemical double layer capacitor (EDLC)	Carbon-based electrodes	EDLC/ non-faradaic process	Good cyclic stability, good rate capability	low specific capacitance, low energy density
Pseudo-capacitor	Conducting polymers or metal oxide	Redox reaction/ Faraday process	High specific capacitance, relatively high energy density	relatively low-rate capability
HSC				

• Asymmetric hybrid (ASC)	Anode: pseudo-capacitance materials, cathode: carbon	Anode: redox reaction, cathode: EDLC	High energy density, high power density, and good cyclability
• Symmetric composite • hybrid	metal oxide/carbon or redox polymer/carbon	Redox reaction plus EDLC	High energy density, moderate cost & moderate stability
• Battery-like hybrid	Anode: Li-insertion material, cathode: carbon	Anode: Lithiation/delithiation cathode: EDLC	High energy density, high cost & requires electrode material capacity match

As mentioned above supercapacitors with all their advantages lack behind in terms of energy density compared to a battery so researchers are constantly putting efforts to solve this issue i.e. to increase the energy density of supercapacitors. There are different strategies available in literature where efforts were made to increase the energy density of the supercapacitor. As mentioned in Eq.2 above that the energy density of the supercapacitor depends on the capacitance and working voltage, so a considerable amount of research was done to enhance the energy density by improving these two factors [7].

The electrode material's high surface area, the presence of pores, and functional groups present at the surface are effective strategies to increase capacitance value. Increasing the specific surface area and controlling porosity in electrode material is related to increasing the capacitance of the supercapacitor, a decent amount of literature is available where these two factors were used to enhance the performance of a supercapacitor.

Wang *et al.* [8] in their work report the high specific surface area impact on the capacitance value of the supercapacitor, furthermore Simon *et al.* in their work showed the importance of attaining optimal pore size for increasing capacitance [9]. The addition of surface functional groups or heteroatoms has shown a significant impact on capacitance value as they are supposed to increase the wettability of the electrode surface and enhance the capacitance generated from a faradic redox reaction. Lin *et al.* in their work reported a high capacitance value of about 885 F/g when nitrogen-doped carbon was used as an electrode material, where it was explained how nitrogen doping turns

carbon into an electrochemically active substance and Chen *et al*. used nitrogen-doped carbon nanofibers as electrode material with the system shows a maximum capacitance value of about 202 F/g [10, 11]. Both of the research showed how doping with nitrogen increase capacity, the surface wettability of materials, and electronic conductivity which eventually improve the overall performance of the supercapacitor.

The increase in the energy density of a supercapacitor is also related to the strategies to increase the working voltage some of the strategies that are available to improve the performance of a supercapacitor using working voltage include using the organic and ionic electrolytes both of these electrolytes have a broad and stable electrochemical window. An asymmetric supercapacitor where two different electrodes are used is also an effective method to increase the voltage window. Ionic electrolyte systems where voltage can reach up to 3 V are one of the techniques to obtain higher energy density in supercapacitors. For instance, Hou *et al*. [12, 13] reported the use of ionic liquid electrolytes in supercapacitors and how it helps in the optimization of pore size which leads to getting higher energy density values. Using HSC is also an effective method used to increase the energy density as it offers a wide operational voltage window. Boruah *et al*. [14] reported the use of tandem asymmetric supercapacitors which showed a high working voltage of 4.5V and 61% higher energy density than a single ASC.

Electrode materials are the most important component in supercapacitors. The selection of electrode material plays a vital role in effecting the overall performance of the device. As mentioned previously as well an ideal electrode material for supercapacitors consists of the following features.

- High surface area
- Controlled porosity
- Desirable electrochemical active site
- High electronic conductivity
- High thermal & chemical stability
- Economical (low cost)

The research on using new and innovative materials for supercapacitors as electrode material is linked primarily to achieving one or more desirable properties as shown above. The properties of

electrode material can be tailored to use it for our advantage during synthesis either through different routes, by doping with different metal ions, or by reducing the size of the electrode material by ball milling which would increase the surface area of the electrode material. This approach to improving the performance of supercapacitors using such electrode materials is the main concept behind this research.

In this thesis, high-performance next-generation supercapacitor devices were assembled using a combination of MXene as one electrode and Manganese-doped zinc oxide nanowires (ZnO NWs), Copper-doped zinc oxide nanoparticles (Cu-ZnO NPs) and Cobalt-doped zinc oxide nanoparticles (Co-ZnO NPs) as another electrode. The following sections introduce the selected electrode material for this research, a thorough literature review of these electrode materials is also provided, and the importance of using these electrode materials is discussed. Metal-doped ZnO has intrinsic and extrinsic defects which in this research were studied, analyzed, and used to enhance the performance of the supercapacitors. The upcoming sections will also introduce the second electrode material which is MXene. MXene is the new family of 2D materials which are gaining great attention as electrode materials due to the advantages they offer. This thesis showed the synthesis route of all the electrode materials used and the characterization techniques to analyze these electrode materials. EPR and photoluminescence spectroscopy are the two major characterization techniques for detecting defect centers due to their superior sensitivity and detection principle. The competing effect of extrinsic and intrinsic defects of metal-doped ZnO and how it affects supercapacitor performance, also when used in combination with MXene as electrode material is discussed. This work also highlighted how different morphology of metal-doped ZnO can affect the supercapacitor performance. The electronic, optical, and electrochemical properties of the electrode material were reported, and the impact of different concentrations of metal ions on the performance of the supercapacitor was shown.

2. ELECTRODE MATERIALS FOR SUPERCAPACITORS

2.1 Zinc oxide (ZnO) as electrode material in supercapacitors

The performance of a supercapacitor is very much dependent on the performance of the electrode materials, therefore the selection of the materials for the electrode is of paramount importance. Currently, carbon electrodes are of most commercial use as they are economical and provide resistance to corrosion. The carbon-based EDLC supercapacitors have excellent cyclic stability and a long service lifetime. However, their performance in terms of capacitance is limited due to the active electrode surface area and pore size distribution. To improve the value of specific capacitance transition metal (TM) oxides were investigated and some of them have shown excellent pseudo-capacitance. From the research of the past few years, transition metal oxides such as RuO_2 [15], Co_3O_4 [16], MnO_2 [17], NiO [18], and ZnO [19, 20] have been considered a potential electrode material for supercapacitor due to their large surface area, control label pore size, good conductivity, high amount of defect structures, relatively high power and capacity [21, 22].

Among the metal oxides available to use ZnO is gaining tremendous attention due to the advantages it offers as an electrode material. ZnO can crystallize in a hexagonal wurtzite structure or a cubic zinc blend. Under normal conditions, ZnO exhibits a hexagonal wurtzite structure as shown in Fig.3.
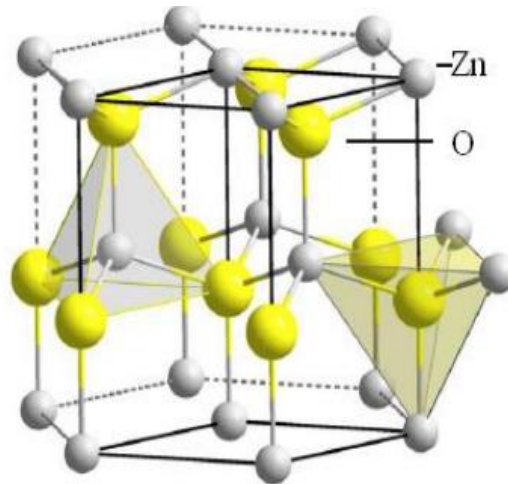
Figure 3: Crystal Structure of ZnO [23].

ZnO is a highly defective semiconductor with a naturally wide band energy of about 3.37 eV at room temperature. ZnO provides increased electrochemical activity, abundance in availability, environmental friendliness, etc making ZnO a popular choice as an electrode material [21, 24-26]. The defective nature of ZnO is one of the primary reasons for using ZnO as an electrode material. Defects in ZnO can be analyzed and tailored to enhance further its performance as an electrode material [27]. The intrinsic defects in ZnO are usually zinc vacancy (V_{Zn}), zinc interstitial (Zn_i), oxygen vacancy (V_O), and oxygen interstitial (O_i). The intrinsic defects in ZnO have been studied thoroughly and an effective core-shell model is developed which will be discussed in detail in the results section.

With the aid of advanced characterization techniques, one may get valuable information on site symmetry, atomic bonding, and, in particular, the bandgap energy of semiconductors. Raman, photoluminescence and electron paramagnetic resonance (EPR) spectroscopy techniques are among the most powerful techniques to extract detailed information on the defect structures of ZnO. Also, electrochemical impedance spectroscopy (EIS) and cyclic voltammetry (CV) are sensitive to electrical properties such as specific capacitance and impedance, which can be correlated with the existence of the defects. Owing to the extreme sensitivity of EPR spectroscopy (10^{11} spins/g) to paramagnetically active defect centers, one may correlate the information on the local electronic configuration from EPR spectra with Raman and PL spectra. The following sections provide in-depth discussions of these mentioned techniques and how they play an important role in understanding the defect environment of electrode material.

The defects in the ZnO lattice can be used to further enhance the material performance. Although, this enhancement can be correlated to different materials characteristics, such as nanoscale size effects, doping, the synergy between the defective electrode and the counter-carbonaceous electrode, and as well as the existence of defects. Doping of ZnO is also a productive option to increase the performance of supercapacitor devices. ZnO is doped with other metal ions and doping of ZnO improves the electrical and optical properties. For example, doping with metal ions develops a point defect in the ZnO lattice, which becomes very useful in the accumulation of charges and assists in forming the intrinsic defect. These intrinsic and extrinsic defects in lattice increase the electrochemical performance of the material. Different metal-doped ZnO had already been reported in the literature used in supercapacitor applications and showed promising results [28].

2.1.1 State of the art of ZnO as electrode material

Researchers have used ZnO with different combinations of material as electrode material in supercapacitor applications and reported their performances. The materials used with ZnO can be broadly divided into three categories Carbon/Carbon related materials, Metal-doped ZnO, and ZnO with different material combinations.

2.1.1.1 Carbon/Carbon-related materials

ZnO was used in combination with carbon or carbon-related materials. As the combination of ZnO with carbon provide Faradic and pseudo-capacitance to the system, this electrode system is really popular in supercapacitor application. Some of such work is shown below.

Li *et al*. [29], reported synthesized three-dimensional (3D) ZnO/rGO/ZnO sandwich-structured (where ZnO is zinc oxide and rGO is reduced graphene oxide) by adding ZnO powder to the reaction of graphitic oxide reduction. ZnO/rGO nanocomposite is formed, and it was reported that the sandwich structure offers a high specific capacitance value of about 275 F/g and good cyclic stability. Methods like cyclic voltammograms (CV), galvanostatic charge/discharge, and electrochemical impedance spectroscopy were used for the performance analysis of the electrode on the supercapacitor. Significant enhancement has been reported for the electrochemical performance of the nanocomposite electrode compared to the rGO sheet used individually. Pant *et*

al. [21], reported a combination of electrospinning technique and hydrothermal process to fabricate ZnO nano-flakes wrapped carbon nanofibers (CNFs), (ZnO/CNFs) composite as an effective electrode material for supercapacitor. Carbon nanofibers possess properties such as excellent conductivity, thermal and chemical stability, and ease of fabrication. The addition of ZnO in CNFs provided benefits like the faradaic capacitance of the metal oxide and the double-layer capacitance of the CNFs with a large specific surface area, which increased the capacitance and energy/power capabilities of the resulting composite. The research reported that the nanocomposite exhibits superior properties compared to pristine ZnO nanofibers. The specific capacitance value reported here is 260 F/g at the scan rate of 5 mV/s by CV. which is far better than the performance of pristine ZnO nanofibers. Kalpana *et al.* [30] used ZnO/carbon aerogel (CA) composite electrodes in a supercapacitor application. ZnO was synthesized by a co-precipitation process. carbon aerogel has a high specific surface area, good chemical stability, and good conductivity as reported. Using carbon aerogel with ZnO would utilize both the faradaic capacitance of the metal oxide and the double-layer capacitance of the carbon. The maximum capacitance of the ZnO/CA supercapacitor was 500 F/g at 100 mA/cm^2. Enhanced value of capacitance was reported in this paper by using the selected materials, The combination of high surface area carbon aerogel with a large specific capacity of ZnO resulted in utilizing both the faradaic capacitance of the metal oxide and the double-layer capacitance of the carbon. Rajeswari *et al*. [31] reported a method to synthesize graphene-ZnO composite electrode material for supercapacitor applications through the hydrothermal method. The addition of graphene can improve the overall conductivity of the composite and with that, the electrochemical stability of pseudocapacitive metal oxides can be increased substantially. 719.2 F/g at a scan rate of 5 mV/s was the highest capacitance value reported. The result suggested improved value in terms of electrochemical performance, the research pointed out that improving the super capacitance performances of this electro-active material could be assigned to the increase in conductivity of ZnO and better consumption of graphene sheet. Lee *et al*. [26] demonstrated the synthesis of the ZnO and activated carbon with high specific area composite, and used the composite as electrode material for supercapacitor. Carbon nanofibers (CNFs) possess properties such as excellent conductivity, thermal and chemical stability, and ease of fabrication. The addition of ZnO in CNFs provided benefits like the faradaic capacitance of the metal oxide and the double-layer capacitance of the CNFs with a large specific surface area, which increased the capacitance and energy/power capabilities of the resulting

composite. The composite was synthesized through an in-situ reaction. The maximum value of specific capacitance reported for this composite was 155 F/g. The paper reported the composite to be ideal for commercial use owing to the superior electrochemical properties reported for the supercapacitor including the high value of capacitance and excellent cyclic retention Ghorbani *et al*. [32] reported a unique flexible electrode comprised of sandwich-type ZnO/rGO/ZnO composite, to be used in flexible supercapacitors with high energy and power density. The rGO sheets can act as physical support of metal oxides, channels for charge transport, and current collector, and ZnO nanoparticles are the main sources of charge storage, the composite formed here shows promising reversible charging/discharging ability with typical supercapacitor behavior and high specific capacitance compared to pure graphene and ZnO electrodes. The synthesis of ZnO was done by Sol-gel method, and ZnO was deposited on GO paper using dip coating. 60.63 F/g was the capacitance value reported in the paper at a scan rate of 5 mV/s. Zhang *et al*. [33] use CNT–ZnO nanocomposite as electrode material in a supercapacitor for better results. Ultrasonic spray pyrolysis (USP) was used to deposit ZnO nanodots on CNT. Carbon nanotubes used in electrode material are due to their high conductivity, large surface area, and chemical stability. While the use of ZnO provided pseudo-capacitance, which increases the total capacitance. The maximum value of capacitance reported in the paper was 323.9 F/g and good reversibility in the repetitive charge/discharge cycling test was also reported. Lu *et al*. [34] developed successfully graphene and ZnO films and used them as an electrode in supercapacitor applications. The addition of graphene can improve the overall conductivity of the composite and with that, the electrochemical stability of pseudocapacitive metal oxides can be increased substantially. The synthesis was carried out using ultrasonic spray pyrolysis. Graphene–ZnO composite electrode exhibited a higher capacitance value (61.7 F/g) and maximum power density (4.8 kW/kg). Dillip *et al*. [35] in his study improved the capacitive performance of the supercapacitor by using ZnO nanoparticles anchored to carbon nanofibers (CNFs) electrode, they further report a strategy where oxygen vacancies were induced in the electrode material which further enhances the conductivity and supercapacitive performance of the hybrid. The coprecipitation method was used to synthesize the electrode material. The highest value of specific capacitance reported was 126 F/g with advantages like improved charge transport, a defect-free interface between CNFs and ZnO, and high active surface area which will provide more reaction sites. Lu *et al.* [36] in this work graphene-ZnO nanocomposite was developed to be used as an electrode material for supercapacitor

applications. The composite was synthesized by microwave-assisted reduction of ZnO ions in an aqueous solution with graphite oxide dispersion using a microwave synthesis system. The developed system shows improved electrochemical properties with the highest value of specific capacitance reported being 146 F/g.

2.1.1.2 Transition metal ion doped ZnO

Transition metal ion doped ZnO is also one of the widely used combinations to be used as electrode material. The doping of ZnO with transition metal ions exploits the semi-conducting properties of ZnO and take the advantage of the fact that desired materials properties may be tailored by controlling the defect structure by TM ion doping. So, different researchers have reported some encouraging results of supercapacitors by using metal ion doping of ZnO. Some of the work is shown below.

 Saarenpaa *et al*. [37], aluminum-doped ZnO (AZO) films were studied as an alternative transparent electrode material to indium tin oxide (ITO) inorganic photovoltaic devices. The primary feature of (the AZO) system is that it is cost-effective and provides long-term supply stability. The ZnO films were developed using an atomic layer deposition technique. The current-voltage characteristics of the devices were measured to investigate the possibilities to use AZO electrodes in photovoltaic applications. The paper summarizes the AZO films and shows results comparable to that of the reference device. Takada *et al*. [38] show conductive aluminum-doped ZnO (AZO) was deposited by pulsed laser deposition as top electrodes for chemical solution deposition derived lanthanum modified lead zirconate titanate (PLZT) capacitors. The study shows that the AZO as a top electrode for the capacitor shows better fatigue endurance behavior compared to when Pt is used as a top electrode. Experiments like hysteresis loop, polarization ratio, and fatigue endurance ratio have been performed to compare the two-capacitor performance. Alver *et al*. [39] developed boron-doped ZnO embedded in reduced graphene oxide (rGO) to use in electrochemical supercapacitors. Three types of rGO/ZnO:Boron composite were prepared varying in the concentration of boron. It was reported that boron-doped ZnO shows higher conductivity, high transmittance, and more chemical stability when compared with undoped ZnO. The composite was prepared by hydrothermal process. The maximum specific capacitance value reported in this research was up to 230.50 F/g at 5 mV/s. The research concluded that the value of

specific capacitance increases with the increase of boron doping. Reddy *et al.*[40], reported Nickel-doped ZnO nanostructures for use as electrode material in supercapacitors. A different doping concentration of Ni was used and electrochemical analysis was performed, the highest specific capacitance value reported was 96 F/g with impressive efficiency. Ali *et al*. [41], used molybdenum-doped ZnO nanoflakes developed on Ni Foam as electrode material for supercapacitors, the dopant-based system showed better performance of supercapacitors with enhanced energy density and better cycling stability. The maximum specific capacitance reported for this system is 123 F/g. Angelin *et al*. [42], developed zirconium-doped ZnO electrode material for supercapacitors, the used system showed superior electrochemical activity and was eco-friendly as well. The maximum specific capacitance reported from this electrode system was 518 F/g with excellent capacitance retention.

2.1.1.3 ZnO with different material combinations

This type can be used to report the work where innovative combinations of material were used with ZnO as an electrode material. The work includes the use of carbon or carbon-related material in combination with TM ion-doped ZnO and ZnO with different structures or designs as electrode material.

Samuel *et al*.[43], showed the Manganese doped ZnO as an economical and sustainable electrode material to be used in supercapacitors devices. The developed electrode material was used with CNFs as other electrodes. The assembled device showed a specific capacitance of 501 F/g with a 92% capacitance retention after 10,000 cycles. The developed supercapacitor showed a high energy density value as well. Alver *et al.* [44] synthesized ZnO particles by hydrothermal method using three different precursors solutions namely zinc acetate, zinc chloride, and zinc nitrate for active materials of supercapacitor electrode. The specific capacitance values of the ZnO electrodes obtained from nitrate, acetate, and chloride precursor solutions were calculated to be 5.87 F/g, 5.35 F/g, and 4.14 F/g, respectively. Electrode with good cyclic stability and small decay capacity was also reported in this research. Luo *et al*. [45] report the use of ZnO tetrapods as electrode material for high-performance supercapacitors. ZnO with a wide bandgap, excellent oxide ionic conductivity, and relatively high power and capacity, has considered a potential candidate for the asymmetric supercapacitor. The ZnO tetrapods were developed by using an oxidative-metal vapor-

transport technique. The maximum value of capacitance reported in the paper was 160.4 F/g. The paper suggested that the ZnO tetrapods can be a perfect electrode material for supercapacitors giving the advantage of low cost and superior electrochemical performance. Kim *et al*. [25], synthesized ZnO/activated carbon nanofiber (ACNF) composites for high-performance supercapacitor electrodes. Carbon nano fiber's excellent conductivity, thermal and chemical stability, and ease of fabrication, when combined with ZnO offers faradaic capacitance of the metal oxide and the double-layer capacitance of the CNFs with a large specific surface area, which increased the capacitance and energy/power capabilities of the resulting composite. ZnO/polyaniline (PANI)-based fibers were synthesized by electrospinning both a solution with the desired amount of zinc acetate (10 and 20 wt%) as the Zn precursor and a 10 wt%, PAN polymer solution dissolved in dimethylformamide. Electrochemical measurements of ZnO/ACNFs reveal a maximum specific capacitance of 178.2 F/g and high energy densities of 22.71-17.77 W-h/kg in the power density range of 400 to 4000 W/kg. They reported a drastic improvement in the electrochemical performance of the supercapacitor with ZnO/ACNF composites with well-distributed ZnO on ACNF used as an electrode. Chaudhary *et al*. [46] developed a ternary Au/ZnO/rGO nanocomposite to be used as electrode material in electrochemical storage devices with a superior application. The noble metal like Au in this system supported by metal oxide improve the performance of the pseudo-capacitor as Au nanoparticles can decrease the interfacial resistance between the current collector and the active electrode material which increases the specific capacitance. The synthesis is carried out using the hydrothermal method. The highest value of capacitance reported in the paper was 875 F/g. The result obtained in this research concluded that the ternary nanocomposite electrode has proved to be an effective electrode material for electrochemical devices owing to the high values of capacitance and in addition to those high values of energy and power densities as well.

Table 2: Summary of ZnO-based supercapacitors

Reference	Materials used with ZnO	ZnO Synthesis Technique	Specific Capacitance
[29]	rGO(Reduced graphene oxide)	Commerical	275 F/g
[21]	Carbon nanofibers	Hydrothermal	260 F/g
[30]	carbon aerogel composite	Co-precipitation process	500 F/g
[31]	graphene-ZnO composite	Hydrothermal	719.2 F/g
[26]	ZnO and Activated Carbon	In-situ reaction	155 F/g
[32]	ZnO/rGO/ZnO	Sol-gel Method	60.63 F/g
[33]	Carbon Nanotube	Ultrasonic spray pyrolysis	323.9 F/g
[34]	Graphene	Ultrasonic spray pyrolysis	61.7 F/g
[35]	Carbon Nanofibers	Co-precipitation	126 F/g
[36]	Graphene	Microwave synthesis system	146 F/g
[37]	Aluminum doped	Atomic layer deposition for AZO films. Nothing specific for ZnO synthesis/	N\A
[38]	Aluminum doped	Pulse laser deposition for AZO film deposition.	N/A (performance of capacitor

		Nothing specific for ZnO/	measure in terms of fatigue endurance)
[39]	Reduced graphene oxide / Boron doped ZnO	hydrothermal	230.50 F/g
[40]	Nickel doped ZnO	Ball milling	96 F/g
[41]	Molybdenum doped ZnO	Hydrothermal	123 F/g
[42]	Zirconium doped ZnO	Co-precipitation	518 F/g
[43]	Manganese doped ZnO and CNFs	Solution-phase synthesis	501 F/g
[44]	Mixing ZnO particles with graphite powder and polytetrafluoroethylene (PTFE)	Hydrothermal	5.87 F/g
[45]	ZnO tetrapods	Oxidative-metal vapor-transport technique	160.4 F/g
[25]	Porous-activated carbon nanofibers	Electrospinning	178.2 F/g
[46]	Au/ZnO/rGO	Hydrothermal	875 F/g

2.2 MXene as electrode material in supercapacitors

From modern research a new family of 2D metal carbides, nitrides, and carbonitrides are being used in supercapacitors, these are called MXene. MXene-based electrodes due to their fascinating electrical and electrochemical properties such as hydrophilicity, conductivity, and surface area, the topological structure are getting exceptional attention in energy storage devices research specially supercapacitors [47].

MXenes are the 2D materials synthesized by the extraction of "A" layers from the layered carbides or carbonitrides commonly known as the MAX phases, they possess the structural formula $M_{n+1}AX_n$, where *M* is an early transition metal, *A* is usually IIIA and IV A group elements, *X* is carbon and/or nitrogen and *n*= 1, 2 or 3. A typical representation of selective etching of A layer from the MAX phase is shown in Fig. 4 Some of the research work where different researchers have used MXene as electrode material in a supercapacitor is discussed below [48, 49]. Different types of MXenes have been developed and used for different purposes, in mono transition metal MXenes Ti_2C [50], Nb_4C_3 [51], Mo_4VC_4 [52], etc and some of the MXene has been synthesized using double MXene oxides $Mo_2Ti_2C_3$ [53], Mo_2ScC_2 [54], etc. MXene use as electrode material in supercapacitors has been reported in numerous works of literature, and their role in enhancing the supercapacitor performance is always mentioned. Some of the research work is presented below.
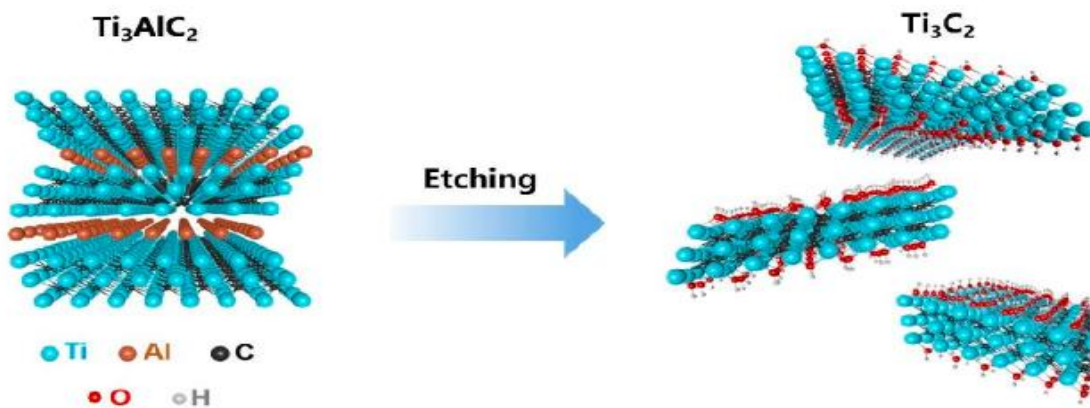

Figure 4: Selective etching of MAX phase to MXene [55]

Xia *et al.* [49] in their work they used a $Ti_3C_2T_x$ MXene electrode incorporated with nickel oxide (NiO) nanosheets, the electrode is synthesized by hydrothermal method. The electrode used in the supercapacitor showed an excellent specific capacitance of 80 F/g and an energy density of 1.04 x 10^{-2} Wh/cm^3. Lin *et al*. [56] synthesized titanium carbide Ti_3C by exfoliation of ternary carbides Ti_3AlC_2 and used them as electrodes in a supercapacitor. The highest capacitance of 117 F/g was reported in this research with high cycle stability and good capacitance retention. Yan *et al*. [57] used a composite material comprised of MXene family Ti_3C_2 and carbon nanotube (CNT) as an electrode material to enhance the performance of the supercapacitor. The result reported shows a high volumetric capacitance of 393 F/cm^3 and increased rate capability and excellent cycling stability. Dall'Agnese *et al*. [58] showed how the electrochemical performance of the supercapacitor was affected by the architecture and composition of the electrode. The electrode material was made up of composite, comprised of Ti_3C_2 along with CNT. The maximum capacitance value of 85 F/g was reported with high-rate capability and good cyclability. Rakhi et al. [48] reported that Ti_2CT_x MXene electrodes were used in supercapacitor devices, and the enhanced performance due to heat treatment of the MXene electrode was reported here. The highest specific capacitance value reported here was 51 F/g, the sample was annealed in N_2/H_2 atmosphere. Fan *et al.* [59] developed MXene and holey graphene films to be used as electrode material in supercapacitors and their electrochemical performance is observed. The MXene/holey graphene film was developed through filtration of alkalized $Ti_3C_2T_x$ MXene and holey graphene oxide (HGO) dispersions. The prepared material when used as a composite film electrode for a supercapacitor shows a high volumetric capacitance of 1445 F/cm^3 with enhanced rate capability and high mass loading. Huang *et al.*[60] reported a comparatively simple processing spray coating approach to massively manufacture the paper-based solid-state Flexible micro-supercapacitors (FMSCs) with sprayable MXene conductive inks. FMSCs are innovative candidates for portable and on-chip energy storage, in this work using the sprayable and immensely conducive $Ti_3C_2T_x$ MXene electrodes further enhanced the performance of the supercapacitor as the high areal capacitance reported was 23.4 mF/cm^2. Zhao *et al.*[61] proposed a simple route for the development of sandwich-like MXene/CNT composite paper electrodes synthesized through alternating filtration of CNT and MXene dispersions. This developed electrode when used in a supercapacitor exhibit improved electrochemical performance compared to pure MXene papers. The maximum volumetric capacitance of 390 F/cm^3 was reported with good electrical

conductivities, high surface areas and mechanical strength. Bayram *et al.*[62] in their work developed a MXene electrode for supercapacitor with architectures that are tunable , and the effect of processing conditions on MXene aerogel architectures which eventually leads to increase in the capacitance of supercapacitor. MXene aerogels that have lamellar structures are fabricated through the unidirectional freeze casting of 2D $Ti_3C_2T_x$ aqueous colloidal suspensions. 380 F/g is the maximum capacitance value showed by the supercapacitor with excellent cyclic stability. Xu *et al.* [63] developed a rGO/ $Ti_3C_2T_x$ MXene based supercapacitor, the rGO/ Ti_3C2T_x films were synthesized using vacuum-assisted filtration of the GO/ Ti_3C2T_x . The supercapacitor developed shows the value of specific capacitance up to 405 F/g. The work reported that the approach used here eliminated the requirement of delamination of MXene and give chance to develop thick electrodes with good electrolyte accessibility.

MXene materials since their origin have successfully shown to possess tremendous potential to be used as electrode material in energy storage devices, the energy storage of MXene material is primarily because of the accommodation of cations between the 2D MXene layers [64]. MXene with the 2D lamellar structure (which helps in cation intercalation that leads to further charge storage) also has good electric conductivity, and surface hydrophilic properties and it can adjust different cations between their layers. Besides all this work, there is still great room available for further research in MXene-related energy storage devices which currently different researchers are working on to further enhance the performance of such devices [47, 65].

3. SYNTHESIS

3.1 Manganese-doped ZnO nanowires

Mn-doped ZnO (ZnO: Mn) nanowires were synthesized using the typical hydrothermal route, by applying some modifications to the process. The precursor materials used were zinc nitrate hexahydrate (ZNH) (Zn (NO$_3$)$_2$.6H$_2$O) from Acros organics, hexamethylenetetramine (HMTA) (C$_6$H$_{12}$N$_4$) from Merk, manganese acetate tetrahydrate (MAT) (C$_4$H$_6$MnO$_4$) from Acros organics, and pure methanol (CH$_3$OH) from Sigma Aldrich.

Equimolar solution of 25 mM of ZNH and HMTA dissolved in de-ionized (DI) water and stirred with an RPM of 500 for 1 h at room temperature in a beaker. In a separate beaker, MAT is dissolved in methanol while continuously mixed until fully dissolved. The two solutions are then mixed and stirred at room temperature and 500 rpm for 10 min. The mixed solution is then placed in a commercial microwave oven and heated for 20 min at 160 W and 800 W microwave power output. The product, white powder is filtered and washed thrice with DI water, once with absolute alcohol to remove any impurities, and dried in the oven at 90 °C for 9 h. Finally, the dried powder is calcined at 300-500 °C for 2 h (depending on MAT mol%). The main control parameters for the synthesis process are MAT mol%, microwave oven power output, and calcination temperature.

3.2 Cu-doped ZnO nanoparticles

The typical co-precipitation method was used to synthesize Cu-doped ZnO nanoparticles. The precursor materials used for the preparation were zinc nitrate hexahydrate (ZNH) (Zn(NO$_3$)$_2$.6H$_2$O) from Acros organics, copper nitrate (II) trihydrate (CNT) (Cu(NO$_3$)2.3H$_2$O), and sodium hydroxide pellets (NaOH) from Sigma Aldrich.

A solution of 3 M NaOH was prepared, dissolving NaOH pellets in DI water and stirring for 15 min at 500 rpm and room temperature until fully dissolved. This NaOH solution was used to control the

pH value of the solution to the desired number. ZNH and CNT are dissolved in DI water (1, 2, and 5 wt %) in a separate beaker and stirred for 15 min at 500 rpm at room temperature until fully dissolved. The NaOH solution is added drop by drop in the mixture of ZNH and CNT to reach a pH of 14. As NaOH solution is added, foam and a blue precipitate can be noticed. Once the desired pH value is reached, the solution mixture is kept stirring at 500 rpm and room temperature for 30 minutes. Finally, the blue powder is filtered and washed thrice in DI water and absolute alcohol. The product powder is then dried at 80 °C for 9 h in the oven.

3.3 Co-doped ZnO nanoparticles

The typical co-precipitation method was used to synthesize Co-doped ZnO nanoparticles. The precursor materials used for the preparation were zinc nitrate hexahydrate (ZNH) $(Zn(NO_3)_2.6H_2O)$ from Acros organics, Cobalt(II) nitrate hexahydrate from EMSURE, and sodium hydroxide pellets (NaOH) from Sigma Aldrich. A solution of 3 M NaOH was prepared, dissolving NaOH pellets in DI water and stirring for 15 min at 500 rpm and room temperature until fully dissolved. To synthesize Co-doped ZnO nanoparticles, Cobalt nitrate was mixed with Zinc nitrate solution following the calculated stoichiometric ratio. The required quantity of aqueous NaOH solution was then added drop by drop to the mixture solution to get (pH ~10). The solution mixture was then stirred at room temperature for about 3 h followed by aging for 24 h at the same temperature. After this step, precipitates that formed were then centrifuged, filtered, and washed several times (distilled water) and were finally annealed at 500 C for 2 h.

3.4 MXene powder & MXene paper

The $Ti_3C_2T_x$ MXene used in this study was synthesized from the Ti_3AlC_2 MAX phases by selective etching of Al atomic layers. In this method, 1 g of Ti_3AlC_2 powder (particle size <44 µm) was slowly added to a solution of 1.8 g of LiF in 20 mL of 9 M HCl acid and etched at 700 rpm for 24 h at 40°Cwith the help of a magnetic stirrer. After etching, this mixture was centrifuged using de-ionized water at 3500 rpm until the pH value was ~6-7, and each cycle, the acidic supernatant was decanted. An ultrasonic sonicator was used for 30 minutes to delaminate $Ti_3C_2T_x$ MXene layers. Then, a

vacuum filtration system with Celgard 3501 separator was used to obtain $Ti_3C_2T_x$ MXene in paper form, while the freeze-drying method was used to obtain $Ti_3C_2T_x$ MXene in powder form.

| Ti_3AlC_2 powder | → | LiF & HCl solution | → | Magnetic Stirrer 700 RPM 24h & 40 °C | → | Centrifuge 3500 RPM | → | Ultrasonic Sonicator (Delamination) |

Ultrasonic Sonicator → Vacuum Filtration system → **MXene Paper**

Ultrasonic Sonicator → Freeze drying Method → **MXene Powder**
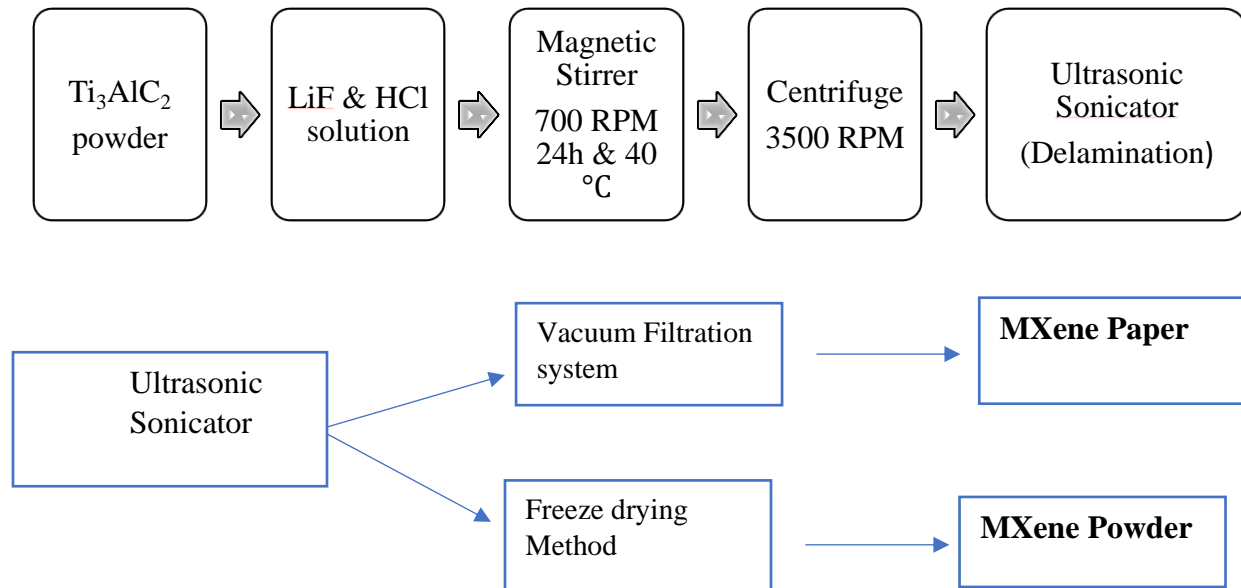
Figure 5: Flow chart of MXene synthesis

4. METHODS

4.1 XRD analysis

X-ray diffraction is a non-destructive method primarily used for the structural analyses of various types of crystalline solid materials including metals, ceramics, and polymers using constructive interference described by Bragg's law [66]. It is used both for qualitative analysis and quantitative analyses of the material. The qualitative part includes identifying the phases and the lattice parameters of the crystalline material where the exact composition is not known, and quantitative analysis has been used to calculate the percentage of crystallinity, the strain, and the relative proportion of the phases in the subjected material.

X-ray diffraction patterns for crystal structure analysis were collected from a Bruker D2 phase diffractometer using Cu Kα radiation ($\lambda = 1.5405$ Å). The 2θ range varied according to the samples, for Mn-doped ZnONW the range was from 25° to 85°, while for Cu-doped ZnONP it was from 20° to 80° and for the MXene sample the range kept from 5° to 85° The XRD results were also used to calculate the average crystalline size using both the Scherrer equation and Williamson-Hall plots.

4.2 SEM analysis

Scanning Electron Microscopy (SEM) is one of the most popular characterization techniques to analyze the morphological and microstructural features of materials. As mentioned in the name SEM uses a focused beam of electrons probing over the surface to gather information and generate the image. The electrons in the beam interact with the sample which then produces various signals that can be used to obtain information about the surface topography and composition.

SEM in this research was used to study the morphological difference of various types of metal ion doped ZnO and the surface features of the MAX and MXene samples. The morphology of samples was observed with the aid of Scanning electron microscopy (SEM) (JEOL, JSM-6010LV) at 5 kV.

4.3 Raman spectroscopy

Raman spectroscopy is a vibrational spectroscopic technique based on the light-matter interaction and the change in polarizability of a molecule during its vibrational motion. The working principle of Raman is that a target molecule is excited by focusing a high-intensity laser beam on it, and induced dipole moments are created due to the interaction of the incident light with the vibration modes of the target molecule. This results in inelastic scattering of light from the molecule, known as Raman scattering which gives information on the chemical and structural properties of the target molecule that is characteristic of each molecular system, therefore represents a fingerprint of the molecule. In this work, Raman spectroscopy was used to investigate the bonding structure and surface chemistry of MXene. The Raman spectra also show the difference in spectra between the MAX phase and MXene which proves the successful etching of "A" layer from MXene. The Raman measurement was performed using the Raman spectrometer (Renishaw inVia, UK) with a 532 nm frequency-doubled Nd: YAG excitation source in combination with a 1200 lines/mm grating.

4.4 X-Ray photoelectron Spectroscopy analysis

X-Ray photoelectron Spectroscopy (XPS) is a quantitative technique that is used to determine the elemental composition of the surface of a material, and it also provides information on the binding states of the elements present. The technique works as the electrons within a sample absorb photons of a particular energy and then come out from the solid. The kinetic energy analysis of emitted electrons from the surface yields information on the electronic states of atoms in the surface region.

XPS in this work is used to gather the surface information of the MXene samples and the surface groups attached to MXene which were used in the etching of MAX phase. XPS Spectra were recorded with a PHI 5000 Versa Probe Instrument equipped with a monochromatic Al Kα X-ray source excited with a micro-focused electron beam.

4.5 Electron paramagnetic resonance spectroscopy

Electron paramagnetic resonance spectroscopy is a powerful tool for studying paramagnetic species like organic and inorganic radicals, and triplet states. The working principle of EPR is very similar to nuclear magnetic resonance spectroscopy (NMR) the difference is that EPR focuses on the interaction of an external magnetic field with the unpaired electron(s) in a molecule instead of the nuclei of individual atoms.

EPR analysis makes them useful in many applications such as in physics, medicine, chemistry, and biology to examine various species, such as free radicals, reaction kinetics, oxidation-reduction processes, conducting electrons, and, here, in particular, point defects. Atoms, ions, or molecules having an unpaired electron in their outermost shells exhibit characteristic electronic properties. EPR takes advantage of the spin magnetic moments arise from the electrons. For an unpaired electron, the spin energy levels are degenerate, and that is electrons spin randomly, without an applied magnetic field. When an external magnetic the field is applied, the spin energy levels split and the spin of the unpaired electron can align with and opposite to the magnetic field, creating two spin states Ms = ± ½. These two spins states have an energy difference between them since they have different energies. This the phenomenon is called the Zeeman splitting (or Zeeman effect).

The energy difference between two energy states can be calculated using the following equation.

$$\Delta E = h\nu = g\beta B_0 \qquad (3)$$

$$g = \frac{h\nu}{\beta B_0} \qquad (4)$$

Where h is the Planck's constant (6.626×10^{-34} J.s^{-1}), ν is the frequency of radiation (s^{-1}), g is the *g*-factor is a unitless measurement of the intrinsic magnetic moment of the electron, β is the Bohr magneton (9.274×10^{-24}, J.T^{-1}), B_0 is the magnetic field (in T).

In this work, EPR is a vital characterization technique that was used to detect the paramagnetic defect center in the metal-doped ZnO samples as these defects are of crucial importance in increasing the performance of the supercapacitor device. Undoped ZnO, Mn-doped ZnO, Cu-doped ZnO, and Co-doped ZnO all have typical EPR signals with a definitive g-factor. In that regard, EPR in this research is also used to confirm the successful doping of ZnO by different metal ions. EPR measurements were carried out using Bruker EMX Nano with an integrated referencing for g-factor, the microwave frequency used was 9.63 GHz. (X-band) and all measurements were done at room temperature with 2 G modulation amplitude and 10 mW microwave power.
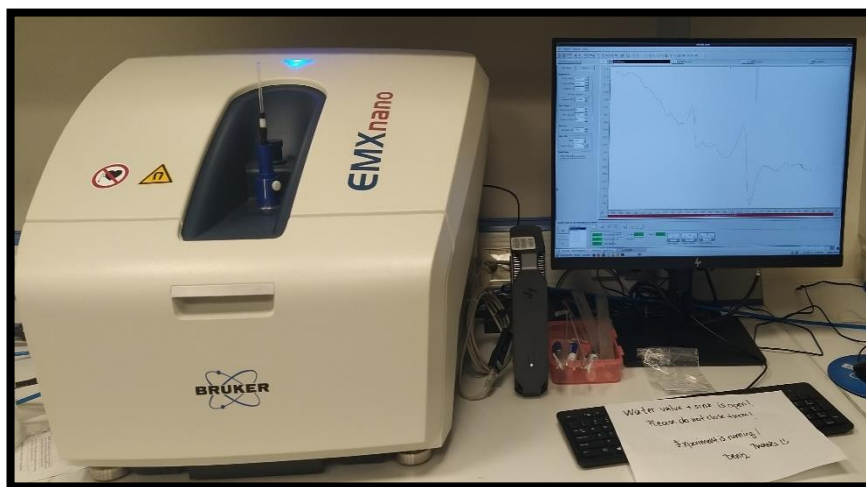

Figure 6: Bruker EMX Nano used for EPR analysis located at FENS lab (2110) at Sabanci University.

4.6 Photoluminescence spectroscopy

Photoluminescence spectroscopy is an efficient optical-based spectroscopy technique. PL is a contactless, nondestructive method of probing the electronic structure of materials. PL provides useful information on the band gap, energy levels, and defects-induced emissions from the sample. Light is directed onto a sample where it is absorbed and exposes excess energy into the material in a process called photoexcitation. One way this excess energy can be dissipated by the sample is through the emission of light, or luminescence. In the case of photo excitation, this luminescence is called photoluminescence.

PL study in this study is used to analyze the point defects induced emission from the sample, the presence of defects was vital for this research. The PL of Mn: ZnO was recorded using a spectrofluorometer FS5 with a 320 nm excitation wavelength with a Xe lamp used as a light source, a 5 nm excitation slit distance, and a 10 nm emission slit distance. The MXene PL spectra were measured on the same instrument with 300nm as excitation wavelength. The Cu: ZnO sample PL measurements were performed by pumping with the 325 nm (3.82 eV) line of aHe–Cd laser chopped through an acousto-optic modulator at a frequency of 55 Hz and a fixed power of 1.5 mW. The PL signal was examined using a single grating monochromator, detected with a Hamamatsu visible photomultiplier, and recorded with a lock-in amplifier using the acousto-optic modulator frequency as a reference.

Figure 7: Spectrofluorometer FS5 for PL analysis located at FENS lab (2110) at Sabanci University.

4.7 Electrochemical analysis

Electrochemical measurements were performed using a Biologic VMP 300 multipotentiostat with the standard two-electrode technique. The electrolyte used for all the test samples was 6M KOH with glass fiber as a separator.

The performance of the supercapacitors and the electrochemical performance of the electrode material was tested using CV, GCPL, and PEIS. CV curves were recorded in a voltage range of 0 to +1 V at a scan rate of 100 mVs^{-1}. PEIS results were completed by applying a sinusoidal signal

of 10 mV from a 10 mHz to 1 MHz frequency range. GCPL was done within a voltage window from -1 to +1 V at a specific current density of 0.10 A g^{-1}, 0.15 A g^{-1}, 0.20 A g^{-1}, 0.30 A g^{-1}, and 0.50 A g^{-1}.

Figure 8: Biologic VMP 300 multipotentiostat used for Electrochemical analysis located at FENS lab (2110) at Sabanci University.

5 . RESULT AND DISCUSSION

5.1 XRD analysis

5.1.1 Mn-doped ZnONW

The structural analysis of the sample was done by XRD analysis. Fig. 9 shows the XRD spectra of the undoped ZnONW and Mn-doped ZnONW samples at 1%, 2%, and 5 % doping concentrations. All the samples showed a typical wurtzite structure of ZnO corresponding to peaks of (100), (002), (101), (102), (110), and (103). These results were expected since Mn^{+2} replaces Zn^{+2} without altering the wurtzite structure due to having a similar ionic radius [67]. The graphs also show that increasing Mn concentrations shift the peaks towards lower 2θ values due to the slight difference between Mn and Zn ionic radius, which are 0.68 Å and 0.75 Å, respectively. An additional peak for a 5% Mn-doped 800 W sample is observed at $2\theta° = 43.5°$ corresponding to $ZnMnO_3$ impurity as explained previously in the literature [68]. The average crystallite size was calculated using Scherrer's equation:

$$D = \frac{K\lambda}{\beta_D Cos\theta} \qquad (5)$$

Additionally, to incorporate the effect of micro strain on the samples Williamson-Hall analysis (W-H) was also performed. The W-H plots are performed by plotting $Cos\ \theta\ \beta_t$ vs. $4Sin\ \theta$, where $\beta_t = \beta_D + \beta_\alpha$ is the total diffraction peak broadening composed of the peak broadening and the broadening due to the micro strain. Table 3 shows the average crystallite size of the Mn-doped samples. The samples synthesized at higher power show a decrease in average crystallite size as the Mn concentration increases, while thew 600W samples an increase in size as the Mn-concentration increases. The difference in the behavior of both samples can be attributed to different reasons which can take the research in a new direction but for this work, these results complement the other characterization results by suggesting that the doping is successfully taking place in the samples and concentration is affecting the lattice structure of ZnO.
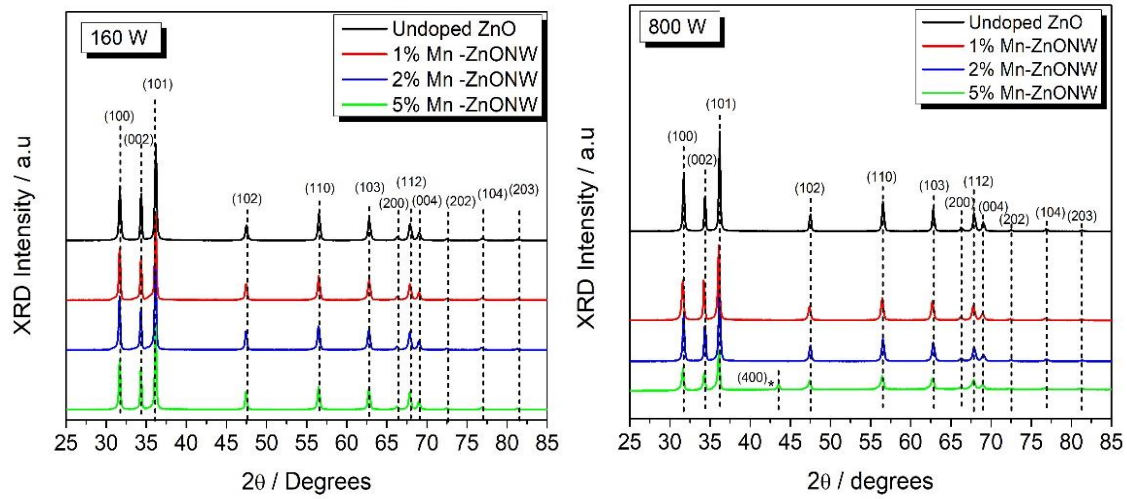
Figure 9: XRD pattern of Mn-doped ZnO NW at 1, 2, and 5 % doping concentration synthesized at 160 W (left) and 800 W (Right).

Table 3: Average crystallite size estimation for Mn-ZnO samples

Mn-ZnO 800 W			
[TM] / %	D_S/nm	Strain$_{W-H}$	D_{W-H} / nm
0	32	0.00122	65
2	27	0.00145	57
5	25	0.00097	36
10	20	0.0007	24
Mn-ZnO 160 W			
0	31	0.00163	62.5
2	33	0.00154	68
5	34	0.00154	72
10	36	0.00143	69.5

5.1.2 Cu-doped ZnONP

Fig. 10 shows the XRD for the Cu-doped sample and peaks for the typical wurtzite structure of ZnO. It shows that the Cu has successfully incorporated in the ZnO lattice, and the dopant did not affect the ZnO lattice due to a similar ionic radius Cu^{+2} has a radius of 0.73 Å, and Zn^{+2} has a 0.75 Å ionic radius. An additional peak (111) for 2 and 5 % dopant concentration appears at 38° which is associated with a CuO phase [69]. Table 4 shows the average crystallite estimation of Cu-doped ZnO samples using Scherrer's equation and W-H analysis, the table shows in that increasing the doping concentration the average crystallite size increase. The increase can be due to the difference in Cu^{2+} and Zn^{2+} atomic radii, 0.73 and 0.74 Å.
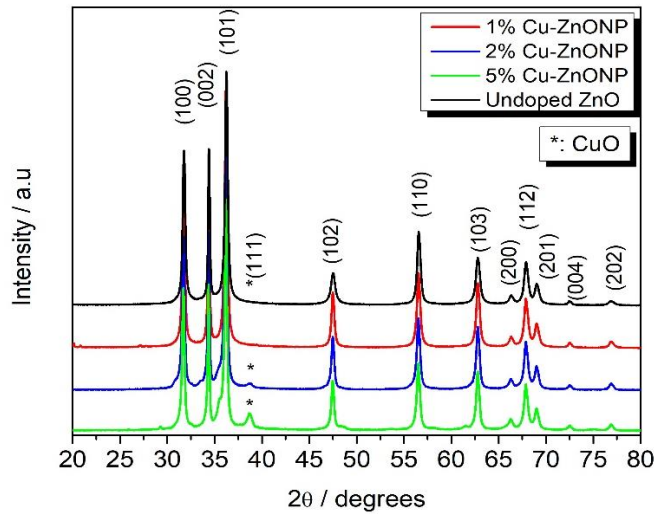

Figure 10: XRD pattern of Cu-doped ZnONP at 1, 2, and 5 % doping concentration.

Table 4: Average crystallite size estimation for Cu-ZnO samples

Cu-ZnO			
[TM] / %	D_S/nm	Strain$_{W-H}$	D_{W-H} / nm
0	23.5	0.0024	56
1	25	0.002	56.5
2	25.85	0.0018	52
5	26.25	0.0018	55

5.1.3 Co-doped ZnONP

Fig. 11 shows the XRD for the Co-doped sample and in this case, also the result suggested successful doping of sample peaks for the typical wurtzite structure of ZnO observed. It shows that the Co has successfully incorporated it into the ZnO lattice. The peak broadening and shifting of the peaks can be observed as the dopant concentration increased which is attributed to the difference in ionic radius of Co^{+2} 0.65 Å, and Zn^{+2} has a 0.75 Å ionic radius. Table 5 shows the average crystallite estimation of Co-doped ZnO samples using Scherrer's equation and W-H analysis, the table shows in that increasing the doping concentration the average crystallite size increased.
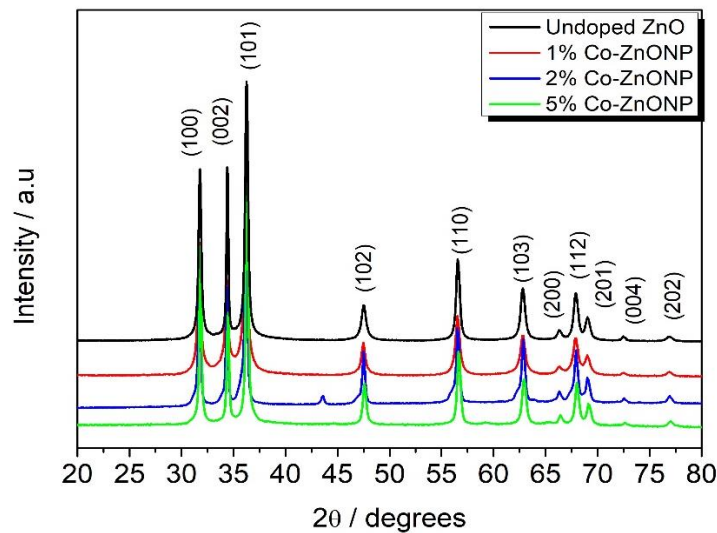

Figure 11: XRD pattern of Co-doped ZnO NP at 1, 2, and 5 % doping concentration.

Table 5: Average crystallite size estimation for Co-ZnO samples

Co-ZnO			
[TM] / %	D_S/nm	$Strain_{W-H}$	D_{W-H} / nm
1	21	0.00596	23.26
2	28.94	0.004175	32.62
5	29.37	0.004254	33.24

5.1.4 MXene powders

Fig.12 shows the XRD pattern for the Ti_3AlC_2 (MAX) and $Ti_3C_2T_x$ (MXene). MAX phase has its primary peak at 9.1° and 19.6° which corresponds to the (002) and (004) respectively [70, 71]. The XRD plot for the MAX and MXene shows that for the MXene sample, the peaks shifted towards a lower angle and a peak broadening of the sample is also visible. This can be attributed to the increase in interplanar spacing of MXene due to the etching of aluminum and the loss of the crystalline nature of the MAX powder [72]. The MAX phase peak at around 38°, which corresponds to the (104) plane belongs to aluminum, and almost the removal of this peak from MXene shows the successful etching of the aluminum layer.
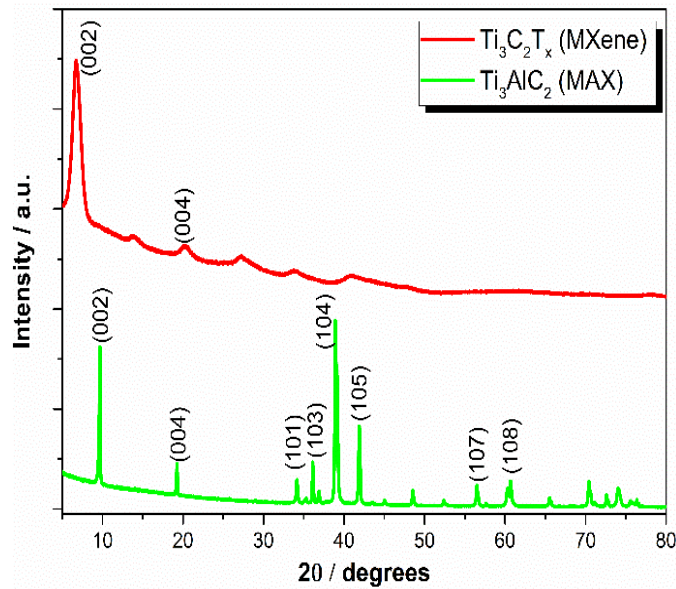

Figure 12: XRD pattern for Ti_3AlC_2 (MAX) and $Ti_3C_2T_x$ (MXene).

5.2 SEM analysis

The morphology of the synthesized metal-doped ZnO was studied by SEM. Fig. 13 (a), (b) and (c) shows how different synthesis route gives different morphology for the metal-doped ZnO. Mn-doped ZnO clearly showed rod-like morphology with an average length of 600 nm and a maximum diameter of 90 nm. A detailed morphological analysis of the Mn-doped ZnO sample is available in our published work [73]. The aspect ratio ($\frac{Length}{Diameter}$) of nanowires samples was also calculated using SEM images, to record the influence of microwave power on the nanowire's morphology. Figure 16 and table 6 shows the obtained result and it was noted that sample made at higher power have denser nanowires means a low aspect ratio. Cu-doped ZnO showed disk-like morphology with rough edges and surfaces and had a diameter of approximately 400 nm and a thickness of about 40 nm. A complete analysis of the Cu-doped ZnO sample is available in our published article [74]. The Co-doped sample showed elongated spherical or near-spherical type aggregates of individual nanoparticles. The obtained morphology is similar to the results available in the literature [75, 76]. Fig. 14 and Fig. 15 show the SEM images of the Ti_3AlC_2 and $Ti_3C_2T_x$ samples. The SEM images show the typical MAX and MXene morphologies, the MAX sample which is without etching shows the stacking of sheets without any space between them. The MXene sample on the other end showed the stacking sheets with space generated between them as the Al is now etched out from the sample generating more space.
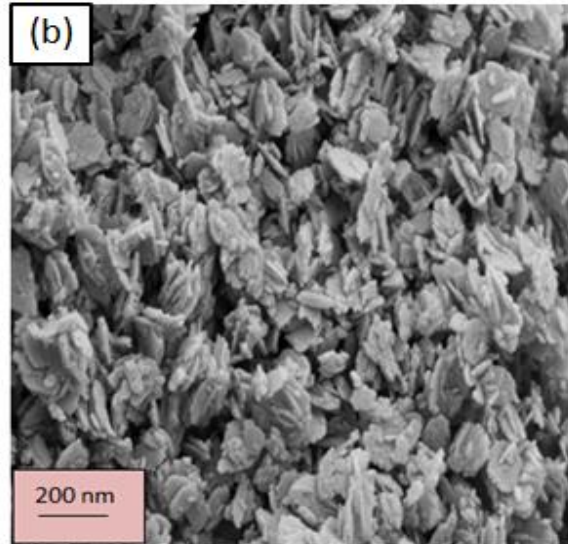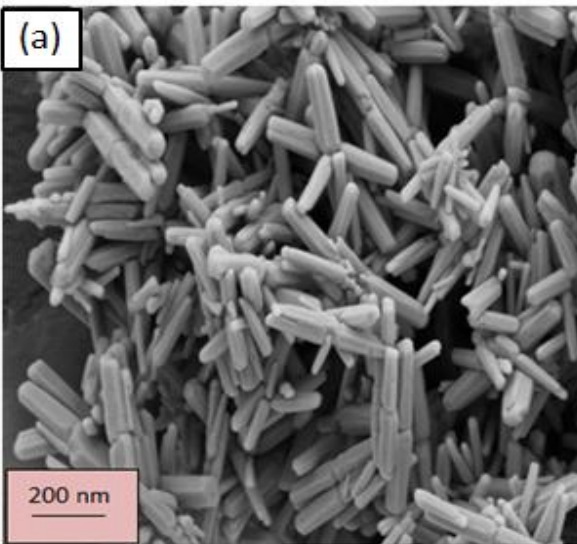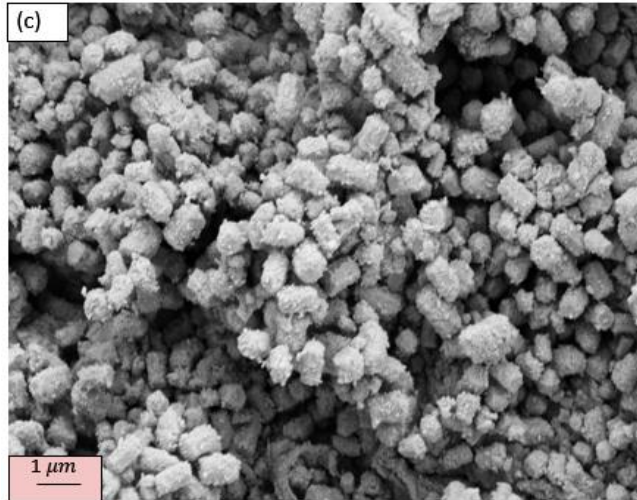
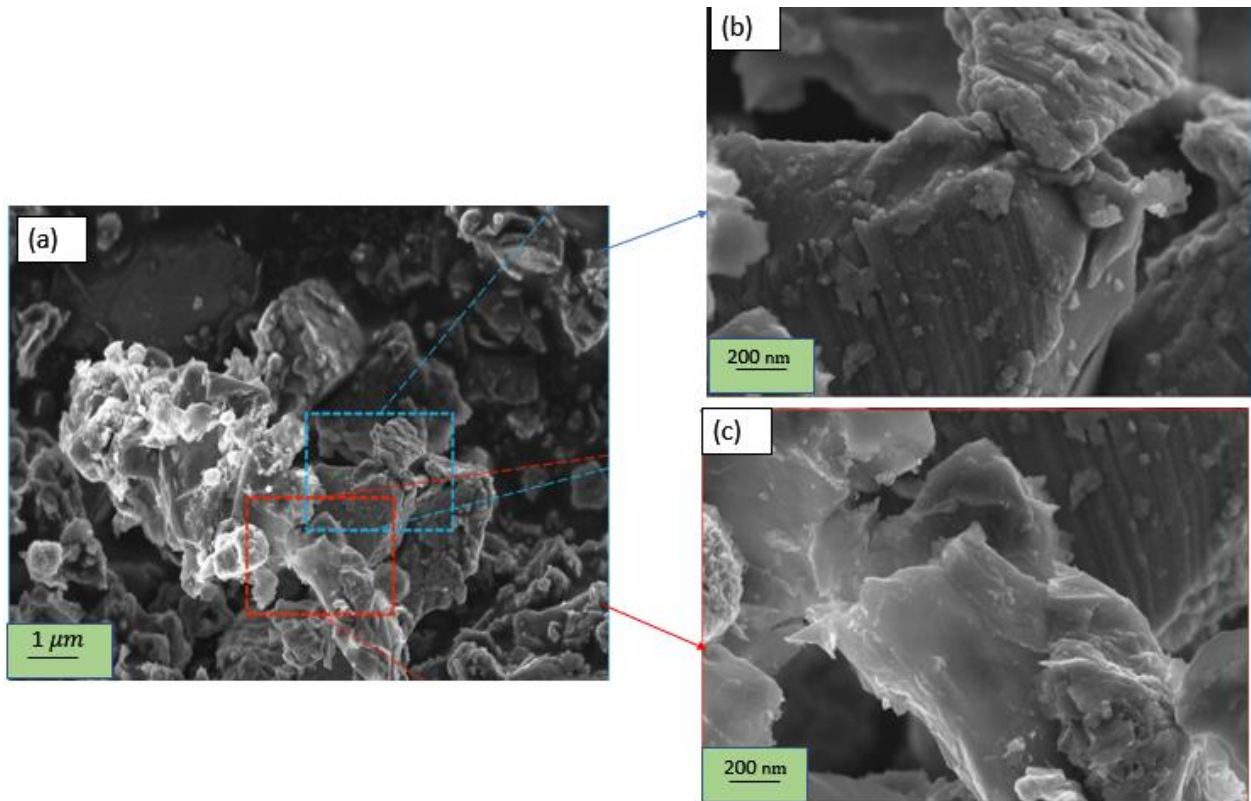Figure 13: SEM images of (a) Mn-doped ZnO NW, (b) Cu-doped ZnO NP, and (c) Co-doped ZnO NP.

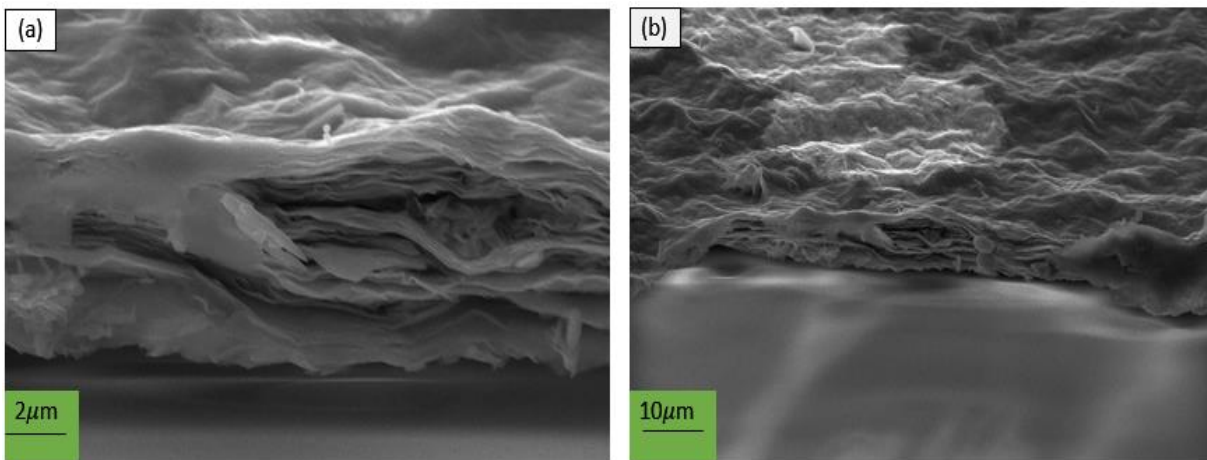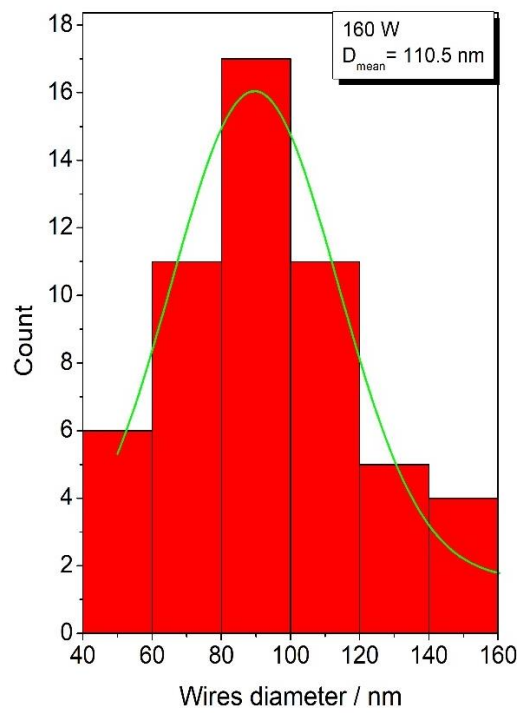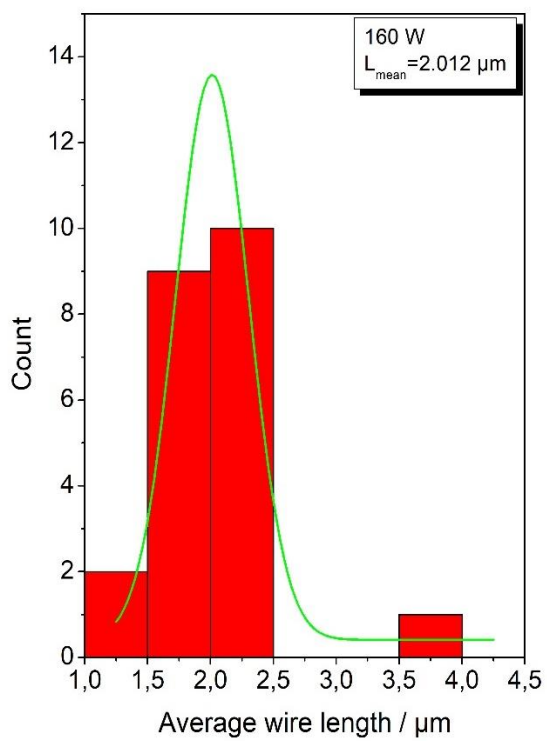Figure 14: SEM images of Ti$_3$AlC$_2$ (MAX Phase).

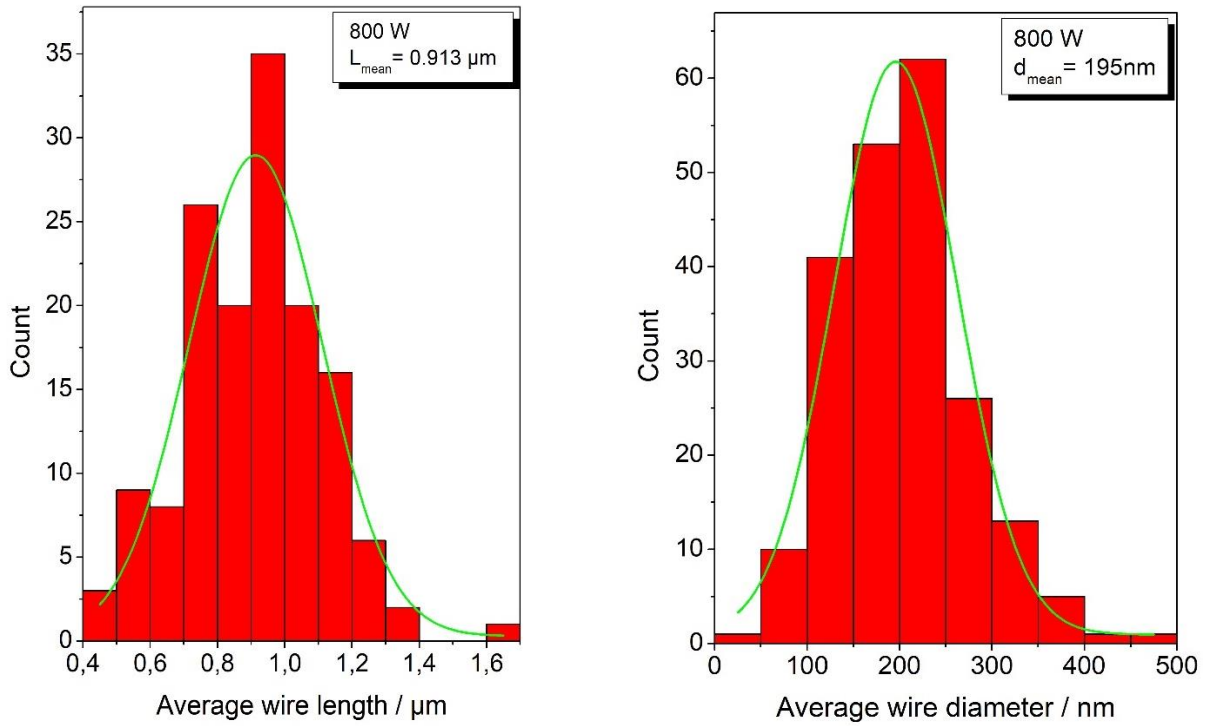Figure 15: SEM images of Ti$_3$C$_2$T$_x$ (MXene).

Figure 16: Aspect ratio histogram of undoped ZnO nanowires

Table 6: Aspect ratio calculation of undoped ZnO nanowires

Microwave power (W)	Average diameter (nm)	Average length (µm)	Aspect ratio
160	110.5 ±2	2.0 ±2	18.2 ±2
800	195.0 ±2	0.9 ±2	4.7 ±2

5.3 Raman spectroscopy

Raman spectroscopy has greatly contributed to the understanding of not only the phonon spectra and structural features of nearly all known 2D materials, but also their mechanical, thermal, and electronic properties. Therefore, Raman spectroscopy emerges as an important analysis method for the characterization of new 2D materials such as MXene. Fig. 17 shows the Raman spectra of the Ti_3AlC_2 starting material in the MAX phase and the obtained $Ti_3C_2T_x$ MXene. It is known that Ti_3AlC_2 (312 phase) belongs to the P63 /mmc space group, and among 33 optical modes, seven Raman-active first-order vibrations ($2A_{1g} + 2E_{1g} + 3E_{2g}$) can be present in this system. However, up to date, only six Raman-active modes have been reported [77]. In the MAX spectrum (Fig. 17), the weak and strong peaks observed around 141, 269, and 601 cm^{-1} were labeled as E_{2g}, A_{1g}, and E_{2g} respectively. These peaks are the key features of Ti_3AlC_2 and match well with those reported in the literature, attributed to shear and longitudinal oscillations of Ti and the Al atoms [77-79]. The weak peak at 141 cm^{-1} is a shear vibration involving the Al and Ti atomic planes. The peak observed at 270 cm^{-1} is likely due to the shear vibrations of the Al atomic planes in addition to the antiparallel shift of adjacent Ti atomic planes [80]. The broad and weak D- and G-bands, which may originate from the sp^2 regions of possible free carbons in the samples, were detected around 1350 cm^{-1} and 1570 cm^{-1} in the spectrum, respectively. While the G-band peak is associated with the stretching of the C-C bond in all sp^2 carbon systems including both rings and chains, the D peak depends on sp^2 fraction and order and appears only if the sp^2 is in disordered rings [81, 82].

In the case of Ti_3C_2, vibrations of this structure can be described as $4E_g + 2A_{1g} + 4E_u + 2A_{2u}$. Among these vibrations, only E_g (in-plane vibrations of Ti and C atoms) and A_{1g} (out-of-plane vibration of Ti and C atoms) are Raman-active. However, it should be kept in mind that lattice vibrations can be affected by the presence of active groups (T_x) on the surface, causing peak shifts and alterations in the spectra. In the MXene spectrum, the peaks at 150 cm^{-1} and 199 cm^{-1} can be assigned to in-plane A_{1g} (Ti, O, and C) modes, while the peak at 424 cm^{-1} was assigned to out-of-plane E_g modes of surface groups attached to Ti atoms [79]. The peak at 614 cm^{-1} can be attributed to both in-plane and out-of-plane carbon vibrations. Similar to the MAX phase, the broad D and G bands at around 1350 and 1570 cm^{-1} were attributed to the presence of amorphous carbon in the MXene spectrum.
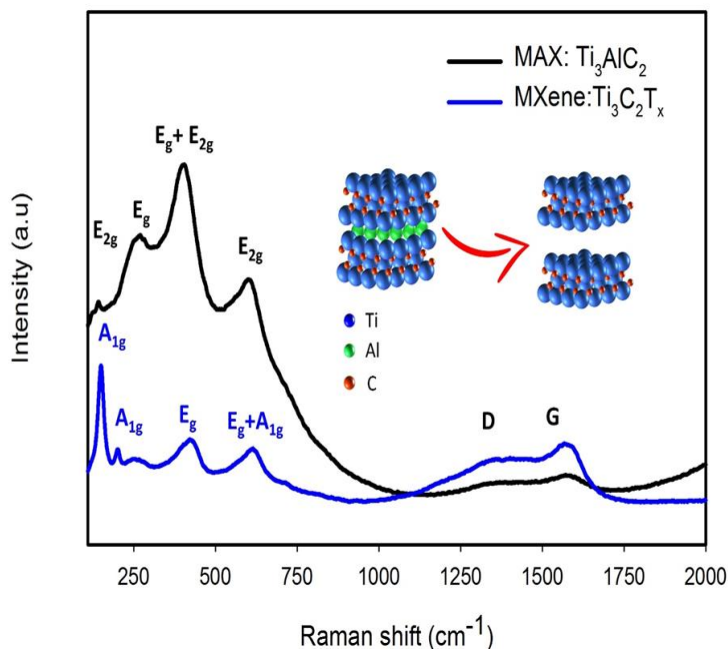
Figure 17: Raman spectra of MAX phase (Ti$_3$AlC$_2$) and MXene (Ti$_3$C$_2$T$_x$).

5.4 X-Ray photoelectron Spectroscopy analysis

To obtain further information on the surface chemistry of the MXene, XPS analysis is performed, and the result is shown in Fig. 18. The graphs showed obvious signals from Ti, C, O, and F elements. High-resolution XPS spectra in the C 1s region (Fig. 18b) of the MXene powder showed four main peaks at 281.8, 285.0, 286.5, and 288.3 eV which originate from Ti-C, C-C, C-O, and C=O/COO-, respectively. The presence of C-O can be attributed to TiO$_2$ and carbon atom networks which may arise due to the oxidation of MXene [83]. Fig. 18c shows the high-resolution spectra of the Ti 2p region which shows peaks when deconvoluted into components corresponding to Ti-C, Ti$_{(II)}$, Ti$_{(III)}$ Ti$_{(IV)}$, and Ti-F. The Ti-C signal is considered to be coming from Ti atoms in the interior of the MXene layers [84-86]. The Ti signal from different oxidation states like Ti$_{(II)}$, Ti$_{(III)}$ Ti$_{(IV)}$ arises from the formation of mixed oxides/fluorides (TiO$_x$F$_y$) and carbon oxides (TiC$_x$O$_y$) showing that the termination of the MXene surface is not homogenous [83]. Fig. 18 (d) shows the high-resolution spectra of O 1s regions which show the presence of Ti-O, Ti-OH, C-O, and C-OH. Fig. 18(e) clearly shows Ti-F which confirms the presence of F groups were present due to etchant.
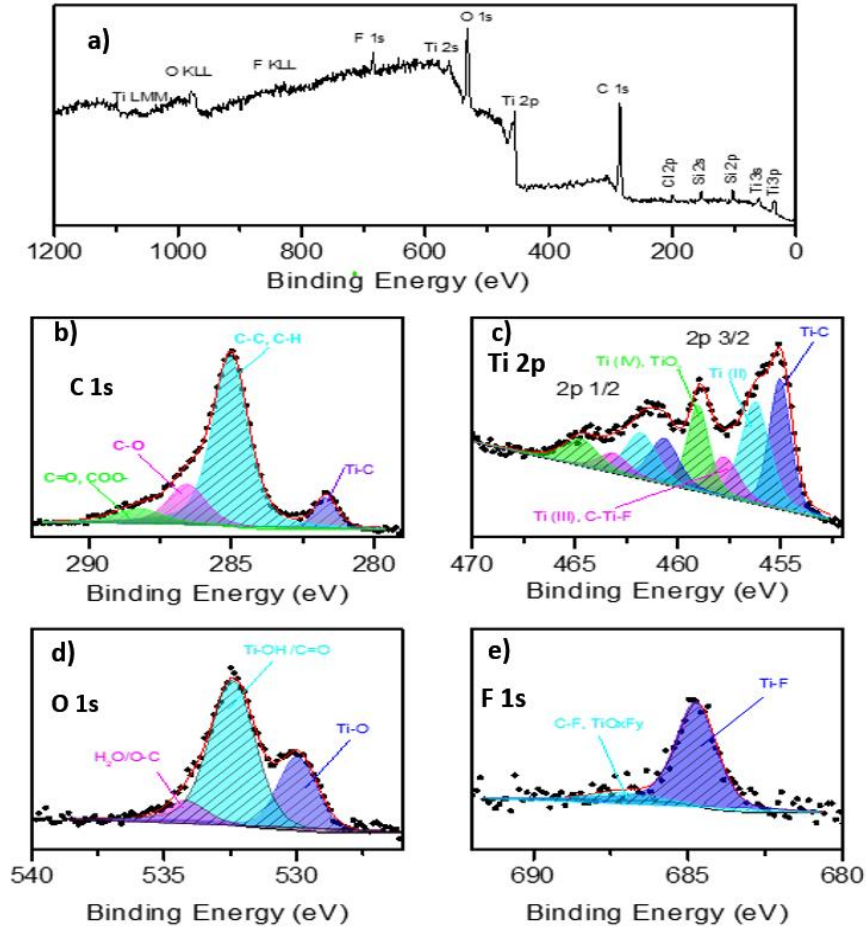
Figure 18: XPS spectra of MXene (Ti₃C₂Tx) powder: (a) survey, (b–e) high resolution spectra of C 1s, Ti 2p, O 1s, and F 1s regions, respectively.

5.5 EPR Analysis

5.5.1 Undoped and Mn-doped ZnONW

The EPR spectra for undoped ZnONW synthesized at 160W and 800W microwave power are shown in Fig.19 we observed two groups of signals attributed to two different defect centers, one of which comes at about g ~ 1.96 and the other at about g ~ 2.02. This is a typical ZnO signal as has explained the nature of these defect centers in literature [87, 88], where a core-shell model has been introduced in the framework of quantum-size effects. The model suggests that the EPR signal at g ~ 1.96 originates from bulk defects (core), confirming that this is coming from the negatively charged Zn vacancies. In contrast, the signal near g ~ 2.02 arises from surface defects (shell), and such defects

have been attributed to the positively charged oxygen vacancies. In this case, due to the high-intensity signal from the core, the intensity of the surface signal is suppressed. The undoped ZnO-NW at 800 W sample shows a lower intensity and a more extensive broadening of the EPR signal than the 160 W undoped sample indicating that increasing the microwave power changes the homogeneity of the defect's centers in the undoped ZnO-NWs. Fig.20 shows the EPR spectra of Mn-doped ZnONW synthesized at 160W and 800W microwave power at 1%, 2%, and 5% of dopant concentration. The spectra show typical anisotropic sextet hyperfine lines of Mn^{+2} indicating the incorporation of Mn^{+2} in the ZnO lattice. Mn^{+2} has only one state of maximum spin multiplicity, S = 5/2 [89, 90]. The spin-orbit coupling split the 5/2 spin into three Kramers doublets, $\pm 5/2$, $\pm 3/2$, and $\pm 1/2$. Six hyperfine transitions arise due to the Mn hyperfine coupling wherein the sextets belong to the transitions $5/2 \leftrightarrow 3/2$, $3/2 \leftrightarrow 1/2$, $1/2 \leftrightarrow -1/2$, $-1/2 \leftrightarrow -3/2$, and $-3/2 \leftrightarrow -5/2$ [67]. The resonant lines show the dominance of Mn^{+2} ions on the intrinsic ZnO defect centers, which almost disappear once the Mn dopant is added. The trend of increase in EPR intensity and broadening of the peaks as the doping concentration increases can be seen in both 160 W and 800 W samples. It can be attributed to the increased Mn^{+2} - Mn^{+2} exchange and spin-lattice interactions with increased doping concentration.
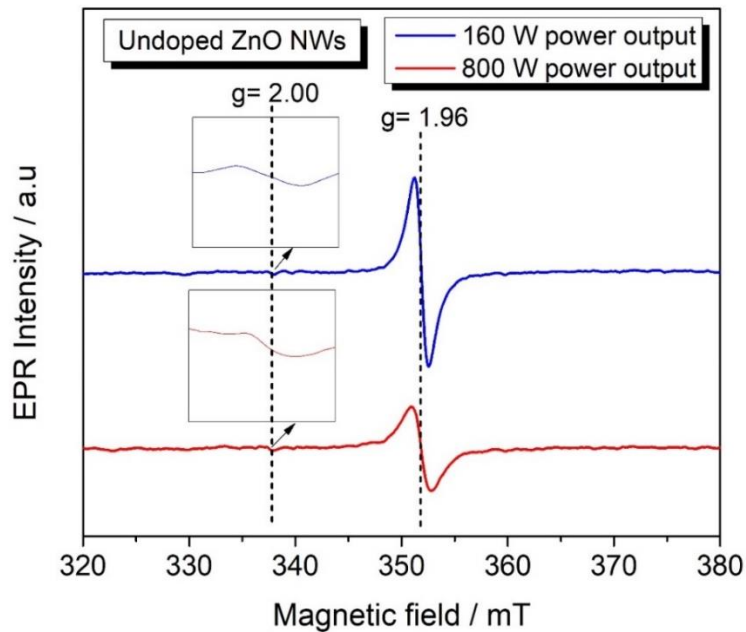

Figure 19: EPR spectra of Undoped ZnONW at 160W and 800W.
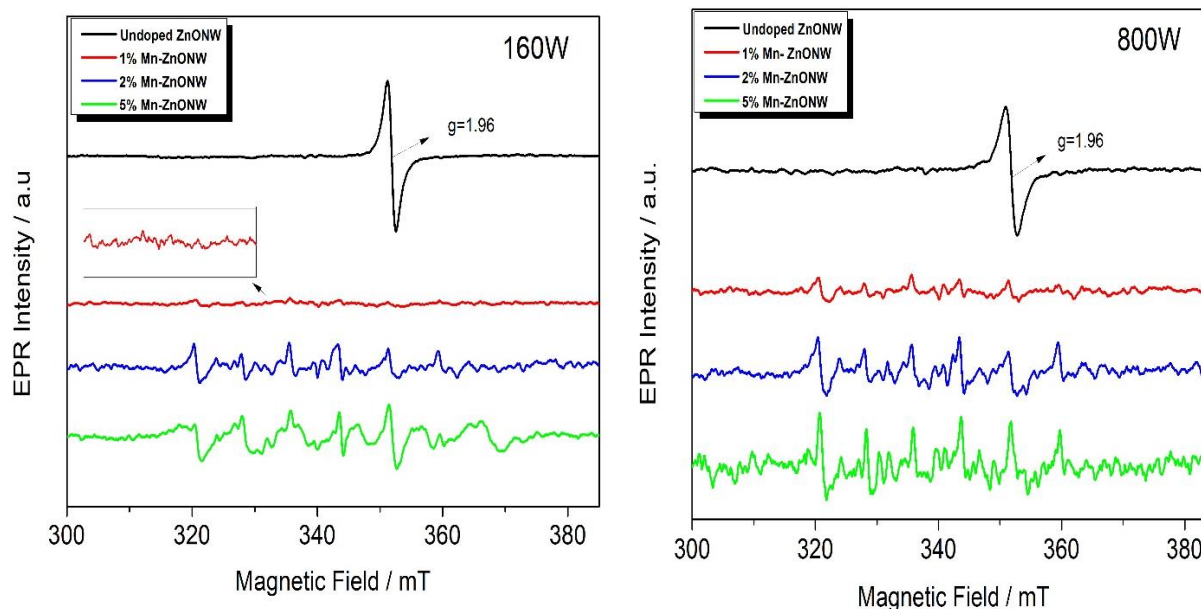
Figure 20: EPR spectra of Mn-doped ZnONW at 1, 2, and 5 % doping concentration synthesized at 160W(left) and 800W (Right).

5.5.2 Cu-doped ZnONP

The X-band EPR spectra of Cu-doped ZnONP at three different concentrations of 1, 2, and 5 mol% are shown in Fig.21. The EPR spectra show the characteristic Cu^{+2} EPR signals with an axial g-tensor and a four-line hyperfine coupling pattern due to the Cu nuclear spin 3/2. The graphs show that as the doping concentration increases, the EPR signal becomes more complex in the high-field region, and a new resonance appears. Although the external defect of Cu^{+2} ions is dominant in spectra, the core and surface signal form ZnO at g=1.96 and g ~2 are slightly visible due to suppressed intensity of external defects.
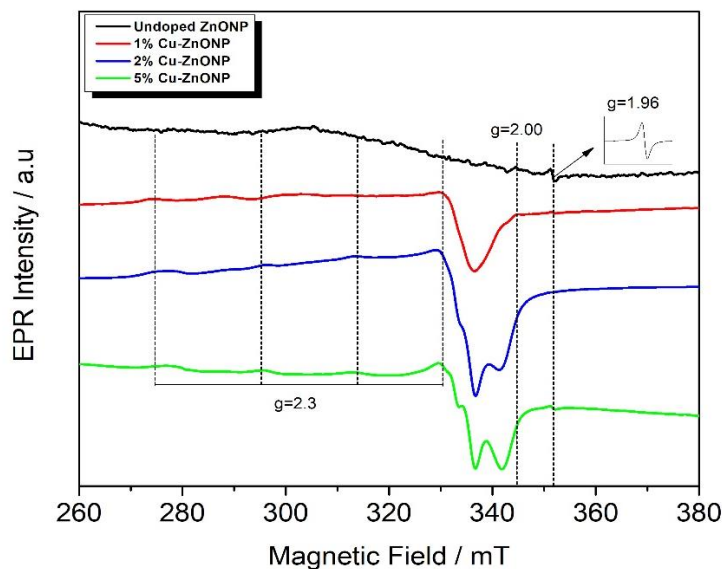
Figure 21: EPR Spectra of Cu-doped ZnONP at 1, 2, and 5 % doping concentration.

5.5.3 Co-doped ZnONP

The X-band EPR spectra of Co-doped ZnONP at three different concentrations of 1, 2, and 5 mol% are shown in Fig.22. The EPR spectra of the Co-doped sample were recorded at 100K. The signals show almost complete disappearance of undoped ZnO core and shell defect signal and in Co^{+2} related signal started to appear at g~2.28 and another signal at g~ 4.56 which is in line with the available literature[91, 92]. The first analysis of the graphs shows that the Co was able to be incorporated within the ZnO lattice and replaced Zn^{+2} intrinsic defect centers. Both the signals have shown an increase in intensity as the dopant concentration increased, which is expected as reported in some previous work. The signal especially at g~ 4.56 was broadened due to crystal-field disorder in all the samples. This disorder is caused by the oxygen vacancies in the second coordination sphere of the Co^{+2} ion which leads to a distribution of zero field parameters[93]. The weak intensity of the g~2.28 signal can be due to the temperature dependence of the Co-doped EPR signal, measuring EPR spectra at an extremely low temperature usually make these signals more prominent.
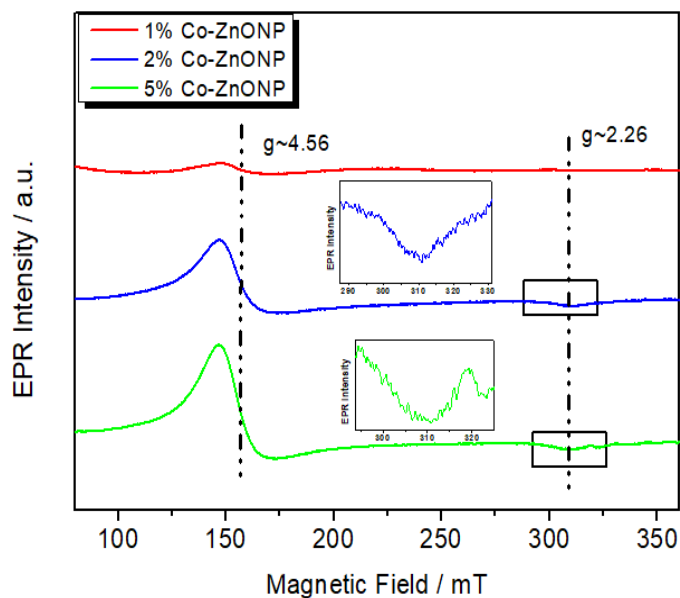
Figure 22: EPR Spectra of Co-doped ZnONP at 1, 2, and 5 % doping concentration.

5.5.4 MXene powder

The EPR spectra of MAX phase (Ti_3AlC_2) and MXene ($Ti_3C_2T_x$) are shown in Fig.23. As expected, both of the samples showed no definite signal are EPR silent. This suggests that there is no paramagnetic defect center in the MXene that can be detected by EPR. Although, the PL spectra of the MXene sample showed defect-induced emission in the visible light region shown in the following section as PL can detect all types of defects, unlike EPR spectroscopy.

Figure 23 : EPR spectra of MAX phase (Ti_3AlC_2) and MXene ($Ti_3C_2T_x$).

5.6 Photoluminescence spectroscopy (PL)

5.6.1 Undoped ZnO nanowires and Mn-doped ZnO Nanowires

The PL spectra of the undoped ZnONW synthesized at 160W and 800W are shown in Fig. 24(a) while the deconvolution of the PL spectra showing different emission regions is shown in Fig. 24(b) and (c). The spectra show the defective structure of both the samples and the results are expected as well as both the samples are in the nanoscale region. The first peak around 380-390 nm represents the band gap energy while the broad peak at a higher wavelength is associated with defect-induced emissions.

Bandgap energies for all samples are estimated at around 3.1 eV, and these results are in good agreement with the typical E_g value of ZnO. On the other hand, the deconvolution of the emission peak in the visible range displays interesting results. A decrease in the green and yellow emissions and an increase in red emissions can be noticed as microwave power increases. Several studies associated the green and yellow emissions with oxygen vacancies V_o, Zinc vacancies V_{Zn}, donor-acceptor pairs, and red emissions to oxygen interstitials O_i and Oxygen vacancies V_O [73, 94, 95]. Figure 25 shows the effect of increasing Mn concentration on the ZnO lattice. Compared to undoped ZnO as we increase the doping concentration, we observed a flattening of the PL emission signal. It represents the intrinsic defects that are suppressed by the dopant addition, indicating that the Mn ions have incorporated the ZnO lattice.

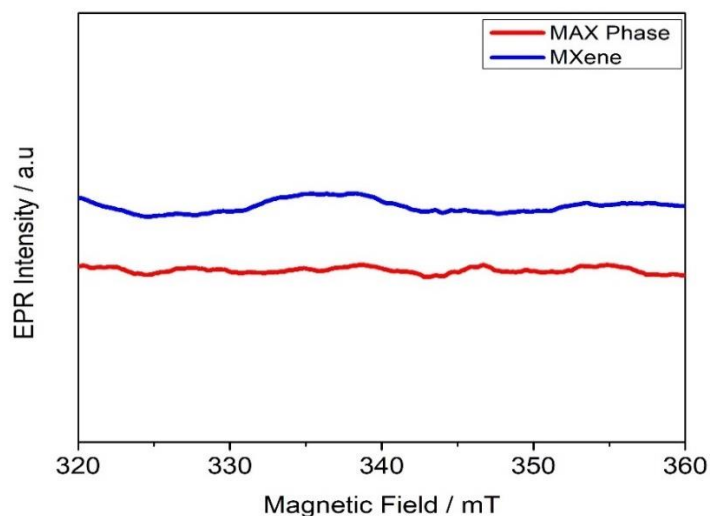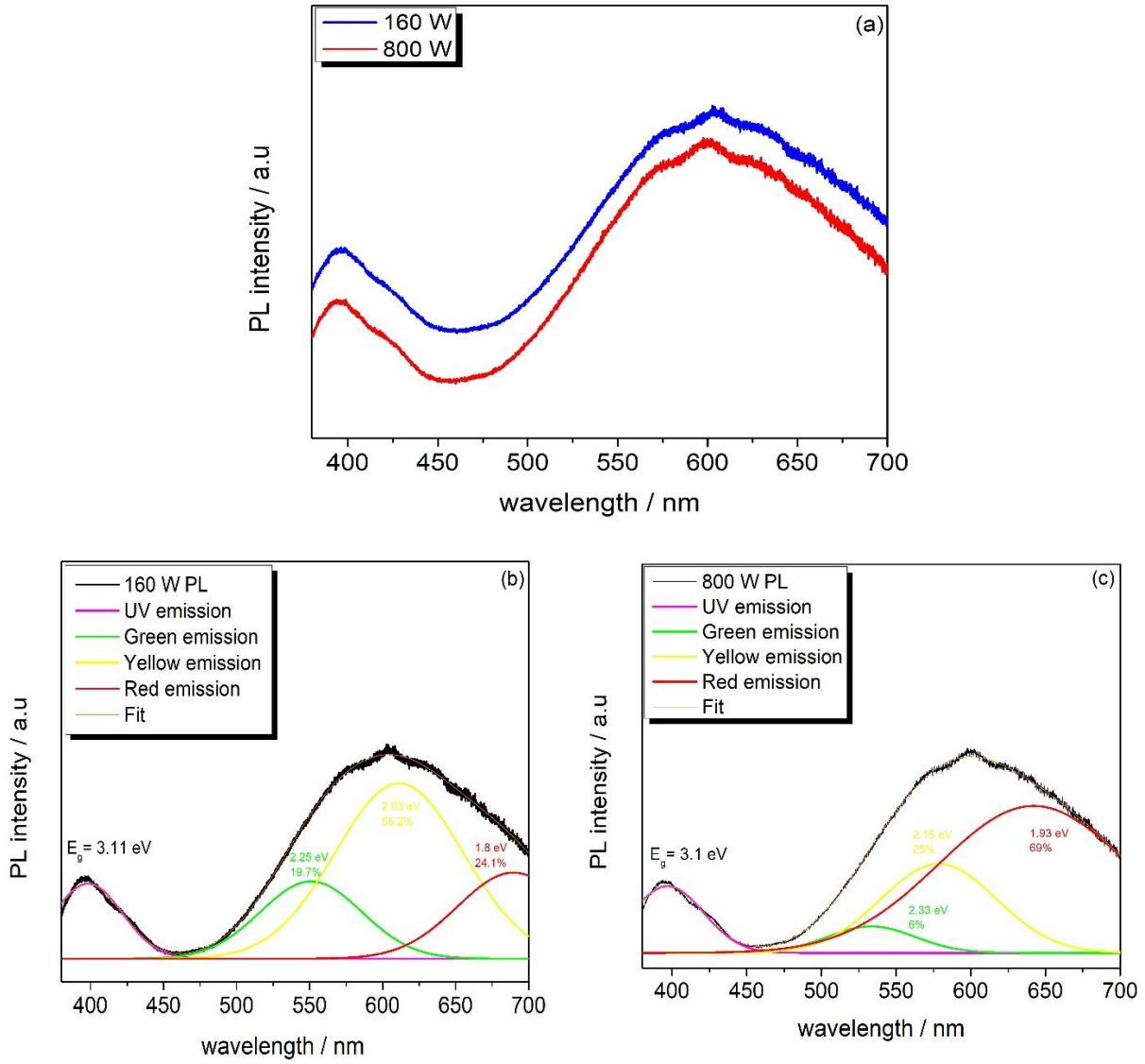Figure 24: (a) PL spectra of undoped ZnONW at 160W and 800W (b) Deconvolution of 160 W PL (c) Deconvolution of 800 W PL.
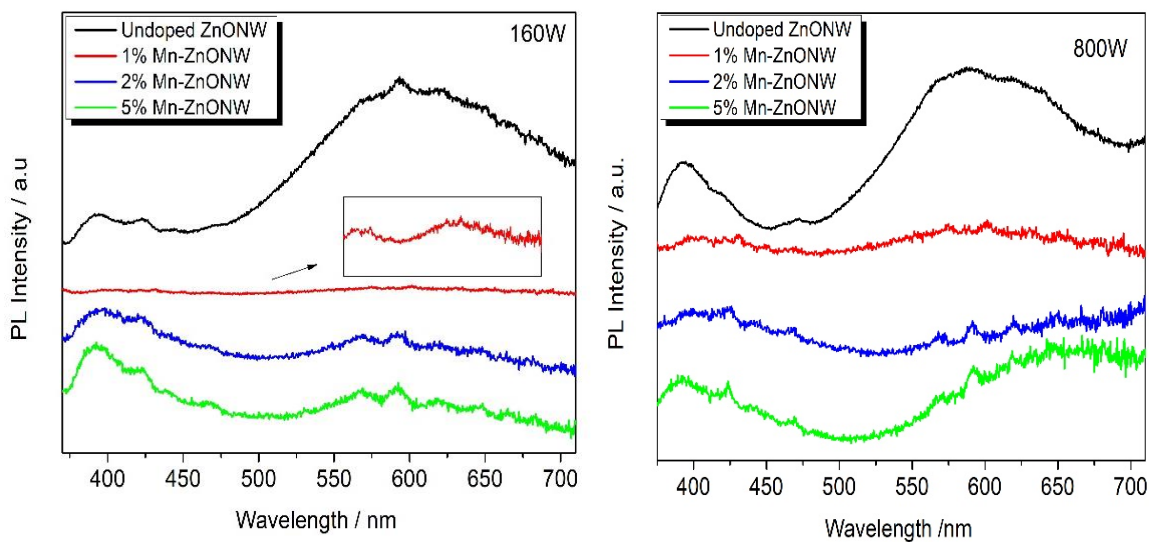
Figure 25: PL spectra of Mn-doped ZnONWs at 1, 2, and 5 % doping concentration synthesized at 160 W(left) and 800 W (Right).

5.6.2 Cu and Co-doped ZnO nanoparticles

PL spectra of Cu-doped ZnONP and Co-doped ZnONP are shown in Fig. 26 and Fig.27 respectively. The trend for both of the samples is the same, observed for both the sample as the dopant concentration is increased the defect-induced emission in the visible light region is suppressed. These results are expected as the extrinsic defects i.e., doping is becoming more dominant on the intrinsic defects of undoped ZnO. These results are well in agreement with the EPR results which also show the competing effect of extrinsic and intrinsic defect centers.
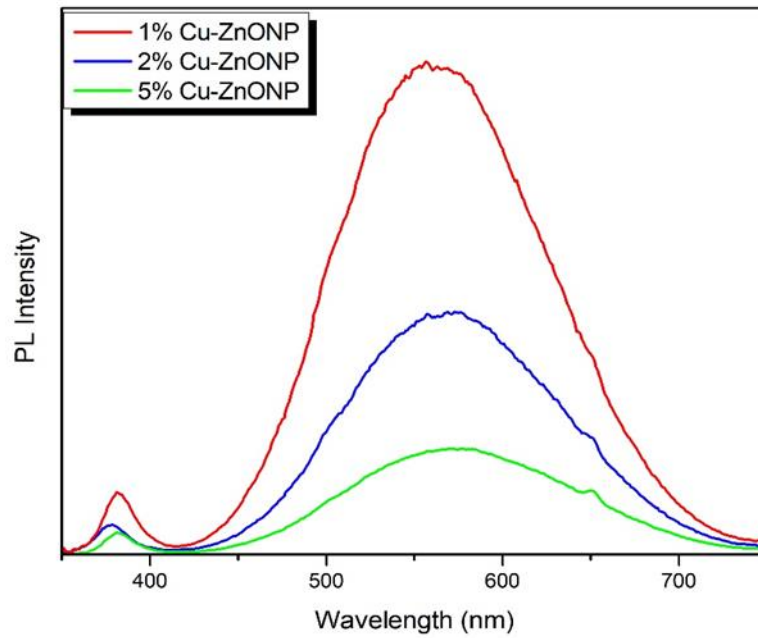
Figure 26: PL Spectra of Cu-doped ZnONPs at 1, 2, and 5 % doping concentration.
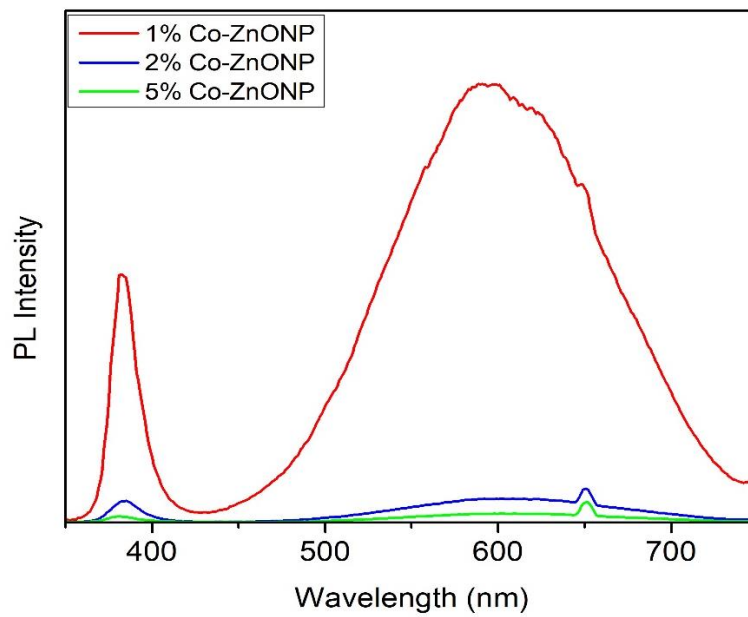
Figure 27: PL Spectra of Co-doped ZnONPs at 1, 2, and 5 % doping concentration.

5.6.3 MXene powder PL analysis

Fig. 28 shows the PL emission spectra of MXene when excited by 300 nm. The spectra showed emissions that peak at ~ 550 nm and this emission signal varied according to the excitation signal which represents that this result is in line with the previously reported results. The small image in the spectra showed the near-band emission of MXene when excited at 300 nm. The PL analysis of MXene showed that there are defect centers in MXene that become the reason for the emission signals, but these defects are not paramagnetic as they were not detected in EPR. The defects signal for MXene like other 2D carbons are controversially discussed and generally, there are two reasons: size effect and surface defects [96, 97].
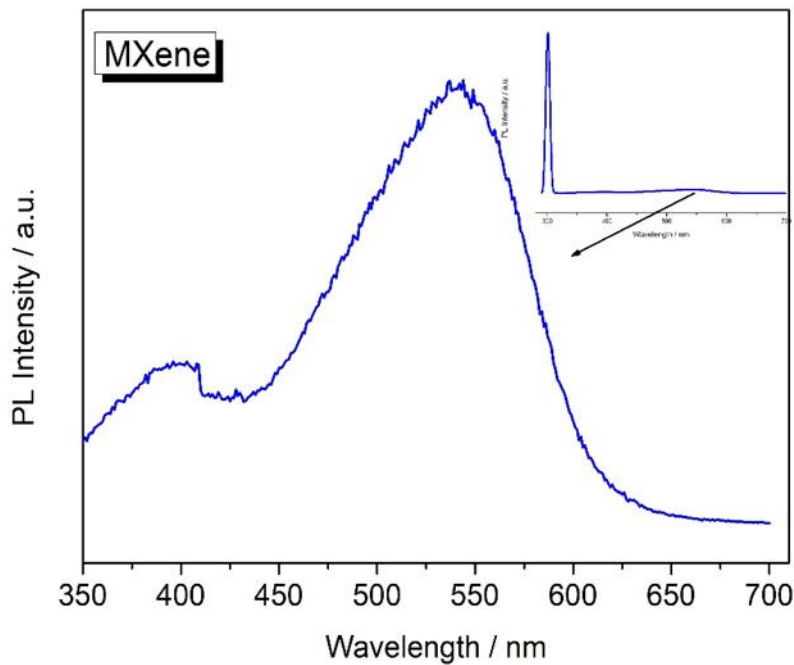
Figure 28: PL emission spectra of MXene excited at 300 nm.

5.7 Electrochemical analysis

The electrochemical analysis of the electrode material was carried out by assembling them into a supercapacitor cell, whose basic design is shown in Fig.29 . The supercapacitor component consists of electrodes on both sides, an electrolyte, and a separator. The comparison of the electrochemical data was performed based on dopant concentration, similar dopant concentration samples are presented together. Tables 7, 8, and 9 showed the supercapacitors designs for metal-doped electrodes with MXene as the other electrode and the results for these designs are shown below. Table 10 showed supercapacitors designs for MXene paper and MXene powder-based electrodes to analyze the electrochemical performance of MXene on its own.
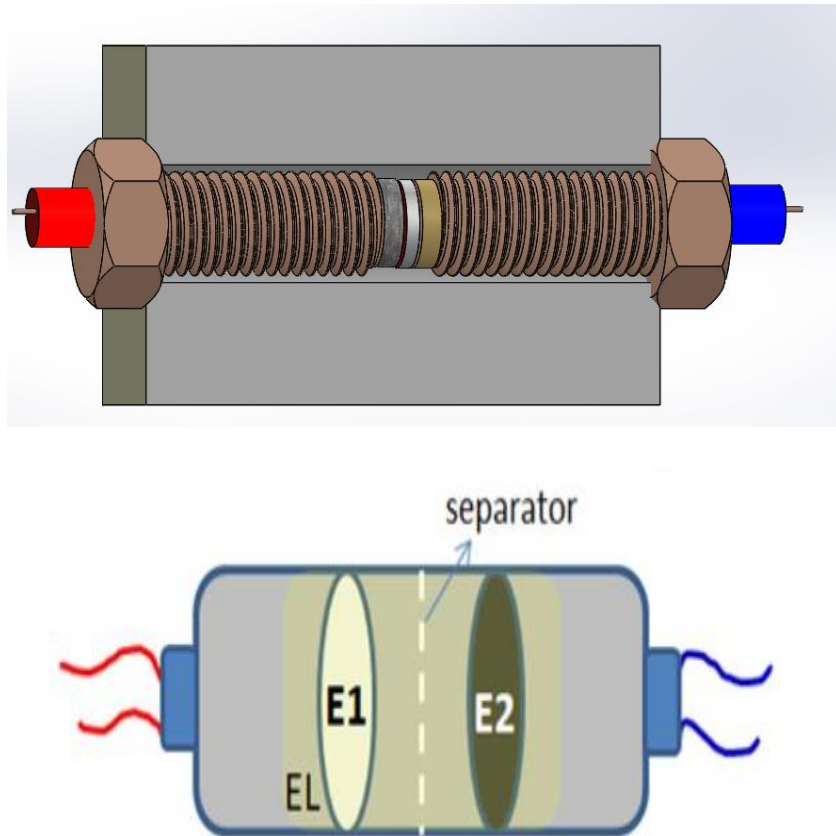
Figure 29: Supercapacitor design and schematic representation.

Table 7: 1% doped ZnO-based supercapacitor design

Electrode 1	Electrode 2	Electrolyte	Separator	Type
1% Mn-doped ZnO NW 160W	MXene Powder	6M KOH	Glass fiber	Asymmetrical
1% Mn-doped ZnO NW 800W	MXene Powder	6M KOH	Glass fiber	Asymmetrical
1% Cu-doped ZnO NP	MXene Powder	6M KOH	Glass fiber	Asymmetrical
1% Co-doped ZnO NP	MXene Powder	6M KOH	Glass fiber	Asymmetrical

Table 8: 2% doped ZnO-based supercapacitor design

Electrode 1	Electrode 2	Electrolyte	Separator	Type
2% Mn-doped ZnONW 160W	MXene Powder	6M KOH	Glass fiber	Asymmetrical
2% Mn-doped ZnONW 800W	MXene Powder	6M KOH	Glass fiber	Asymmetrical
2% Cu-doped ZnONP 1	MXene Powder	6M KOH	Glass fiber	Asymmetrical
2% Co-doped ZnO NP	MXene Powder	6M KOH	Glass fiber	Asymmetrical

Table 9: 5% doped ZnO-based supercapacitor design

Electrode 1	Electrode 2	Electrolyte	Separator	Type
5% Mn-doped ZnO NW 160W	MXene Powder	6M KOH	Glass fiber	Asymmetrical
5% Mn-doped ZnO NW 800W	MXene Powder	6M KOH	Glass fiber	Asymmetrical
5% Cu-doped ZnO NP	MXene Powder	6M KOH	Glass fiber	Asymmetrical
5% Co-doped ZnO NP	MXene Powder	6M KOH	Glass fiber	Asymmetrical

Table 10: MXene-based supercapacitor design

Electrode 1	Electrode 2	Electrolyte	Separator	Type
MXene Paper	MXene Paper	6M KOH	Glass fiber	Symmetrical
MXene Powder	MXene Powder	6M KOH	Glass fiber	Symmetrical
MXene Paper	MXene Powder	6M KOH	Glass fiber	Asymmetrical

5.7.1 Cyclic Voltammtery

Fig. 30 shows the CV curve of all the supercapacitor designs measured at a 100 mV/s scan rate. The graph shows the second cycle of the design except for the MXene symmetric Fig. 30 (d) which shows all 11 cycles, the shape for all of the designs appeared to be conical-tapered deviating slightly from the rectangular shape or else called quasi-rectangular. This shows for all the designs, the charge storage is due to the contribution of both electric double-layer capacitance (EDLC) and pseudo-capacitance (although no redox peaks are observed). The shape of the curve indicated good capacitive behavior of the supercapacitor and a fast charge-discharge process. The nanowire's morphology, in general, showed a higher current value than the nanoparticles' morphology as can be seen in each of the dopant concentration graphs (Fig. 30 (a-c)). However, the 800W Mn-doped sample showed a high current value at each dopant concentration. The reason can be based primarily on the surface area of the electrode material. The high surface area provides more sites for the electrochemical reaction. It has been shown that nanowire morphology proves to be an excellent option for electrochemical reactions to take place. Nanowires as electrode materials provide increased electrochemical active sites for the redox reaction to take place. The nanowire structure increases the wettable surface area and improves the conductivity due to the 1-D structure of the nanowire [98, 99]. It also shortens the transportation pathway length and accelerates the faradic reaction. The highest value from the 800W Mn-doped sample can be attributed to the higher surface area of the 800W sample, the sample synthesized at 800W is denser and has a higher diameter value which results in more electrochemical sites for reactions to take place [99]. Fig. 30 (d) shows the CV curve of the MXene symmetric supercapacitor design with all its 11 cycles presented. The curve

shows the superior performance of this device compared to any other design, as this supercapacitor shows a higher current value of all cycles compared to any other supercapacitor design. Fig. 31 presents the CV graphs of MXene powder and MXene Paper based symmetric and asymmetric supercapacitors. The shape of the CV curves is similar to that of the other design showing both types of reaction, in these cases, MXene powder-based symmetric electrode shows superior performance compared to others.
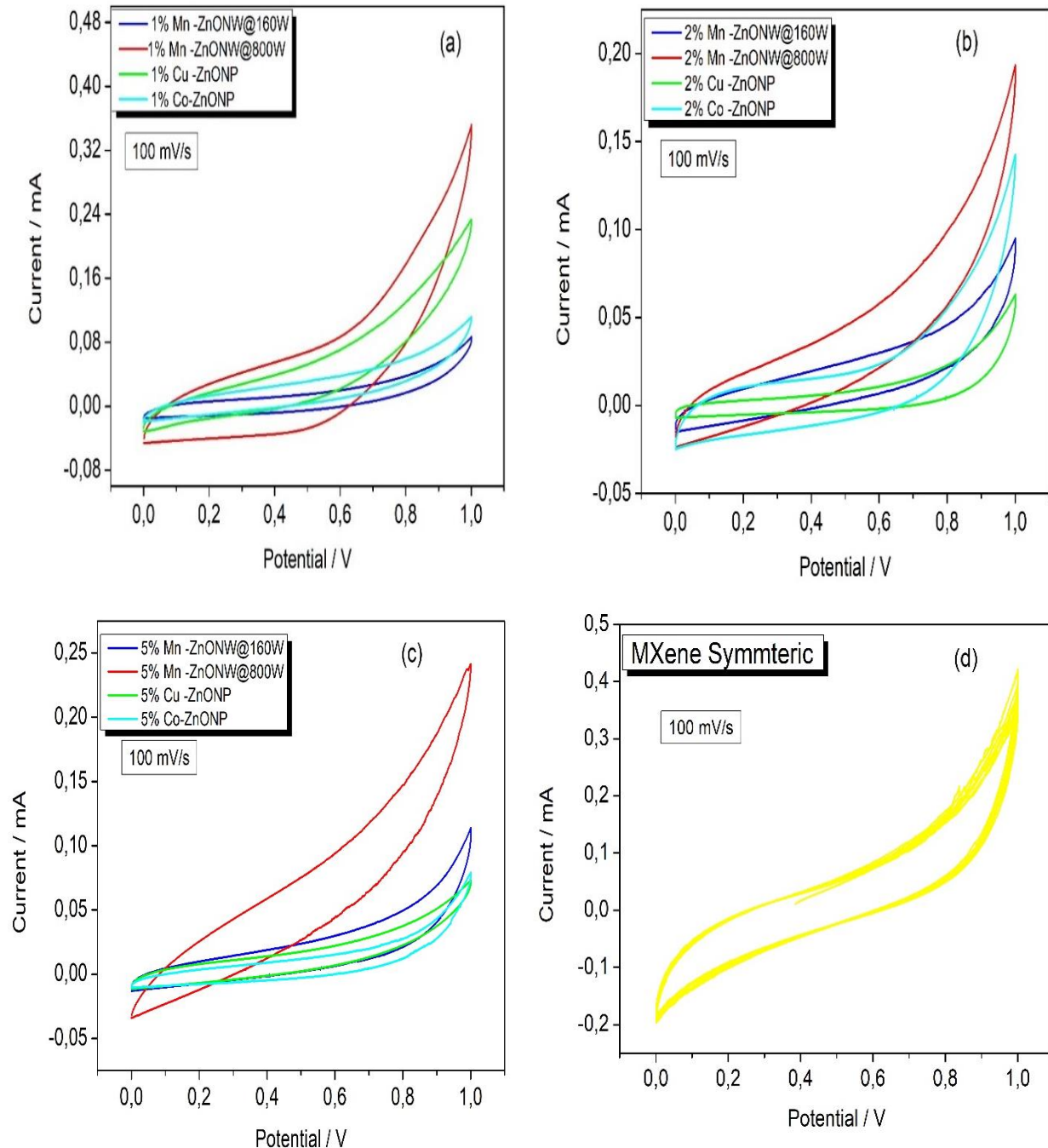
Figure 30: Cyclic Voltammetry scans supercapacitor designs: a) 1% doped samples, b) 2% doped samples, c) 5% doped samples, and d) MXene symmetric.
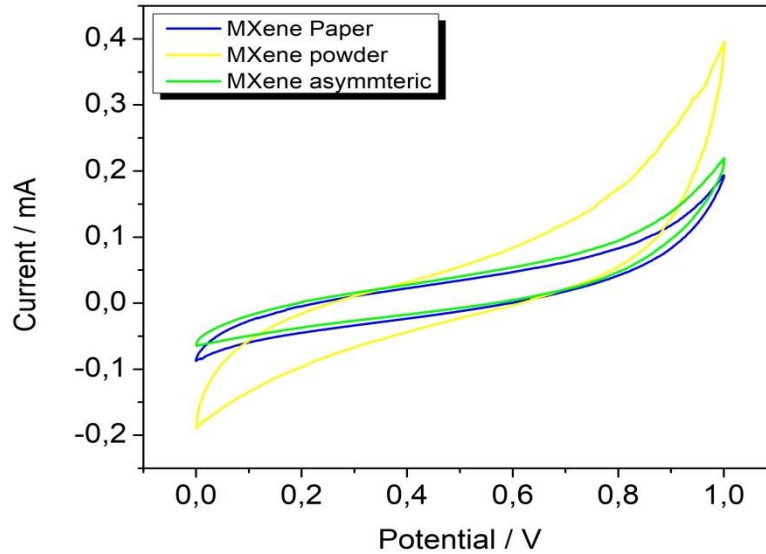

Figure 31: Cyclic Voltammetry scans supercapacitor designs for MXene-based electrode.

5.7.2 Electrochemical impedance spectroscopy

Fig. 32 shows the Nyquist plot for all the supercapacitor design's electrochemical impedance measurements of the system. No semi-circle was observed in the high-frequency region for any of the graphs that indicate fast ion diffusion with no or negligible interfacial charge transfer resistances of the measuring electrodes. The MXene symmetric supercapacitor compares to all other designs shows the lowest value of impedance, which suggests better performance which is like the CV result. The Mn-doped sample of 800 W power in the Nyquist plot in all dopant concentration values showed lower values of impedance in the high-frequency region compared to other asymmetrical designs, although at lower frequency regions we observed different trends in all the graphs. The Cu-doped sample generally showed a lower impedance value than their dopant counterparts in other concentration values. Fig. 33 showed the equivalent circuit fitting of Nyquist plot data for all the doped ZnO samples. The x-intercept in Nyquist plots at high frequency represents the equivalent series resistance (R_S) which corresponds to the resistance of the electrolyte, the contact resistance of the interface between the current collector and the electrode and it also showed the resistance of the active material. Table 11 shows the Rs values of all the

supercapacitor designs. The nanowires samples show lower values of contact resistance and 2% Mn-doped samples at 800 W recorded the lowest value of contact resistance which also has a steeper Warburg slope indicating the increased charge transfer and fast ion diffusion. The constant phase element (Q) present in all the equivalent circuits is to represent the deviation from the ideal capacitance and diffusion behavior due to the non-homogeneity of the surface at the electrode-electrolyte interface. Fig. 34 showed the Nyquist plot for MXene paper and MXene powder-based symmetric and asymmetric supercapacitors. The result was consistent with the result obtained in Fig. 31. MXene powder-based symmetric design showed the lowest value of impedance showing its superior electrochemical performance. MXene paper-based supercapacitor design showed higher impedance and semicircle at a high-frequency range suggesting slow diffusion of ions.
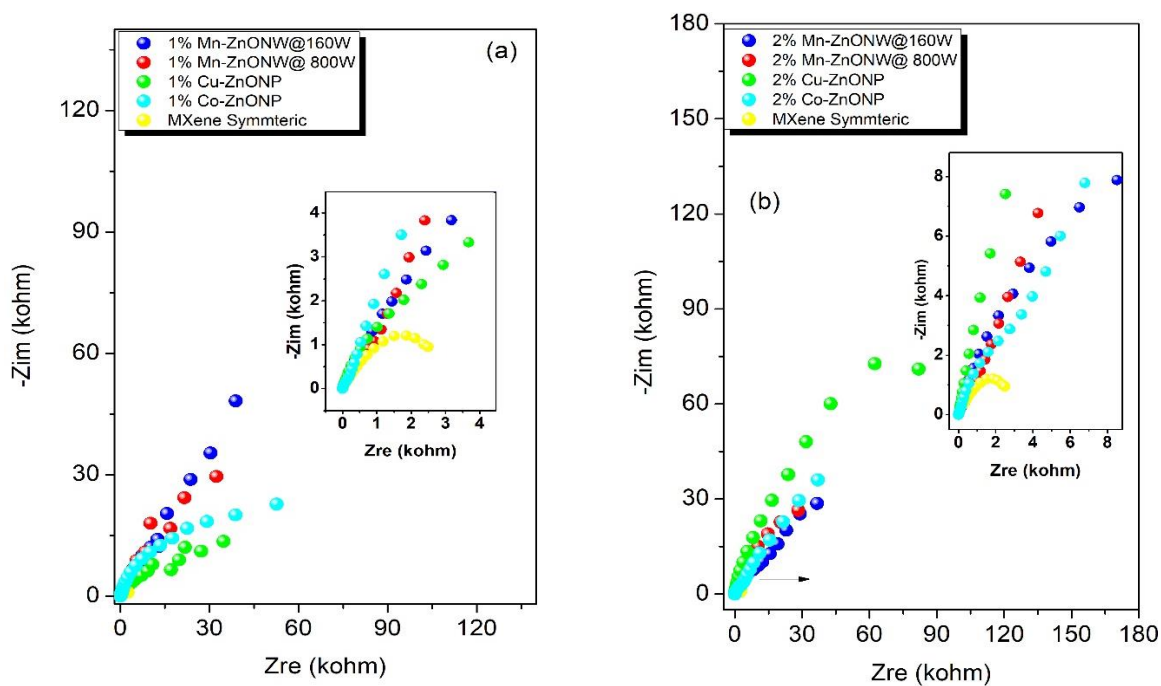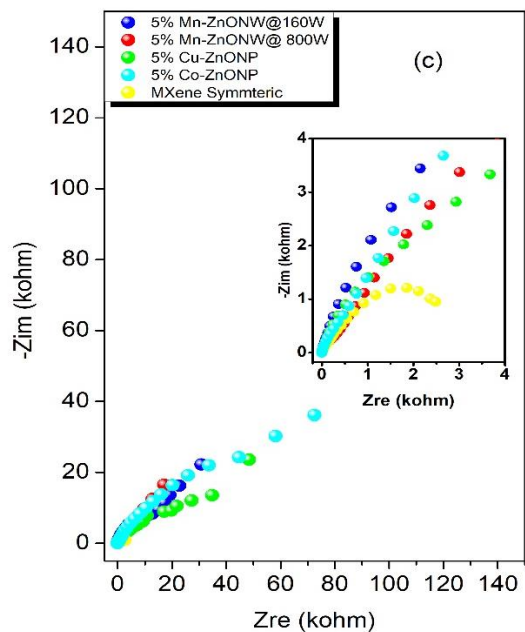
Figure 32: Electrochemical impedance spectra (Nyquist plot) of supercapacitor designs: a) 1% doped samples b) 2% doped samples and c) 5% doped samples.
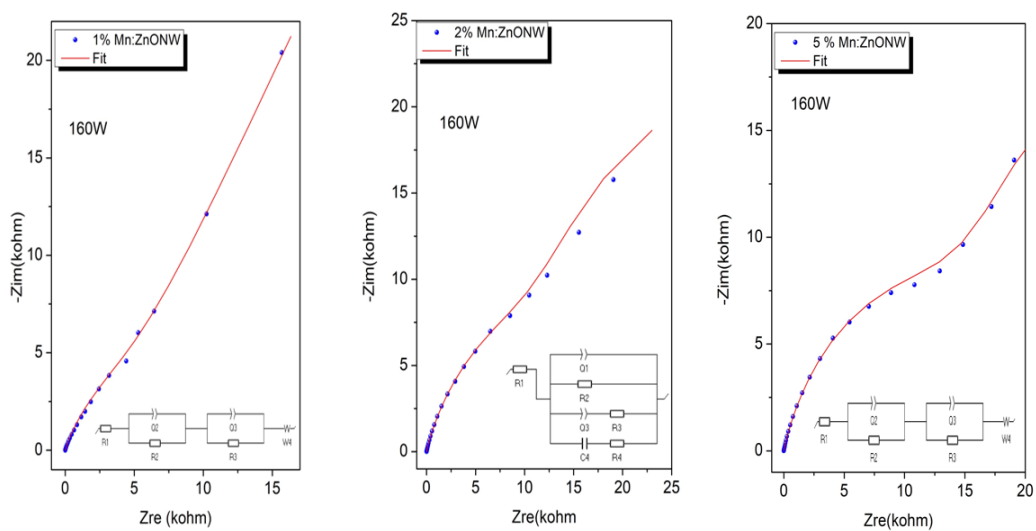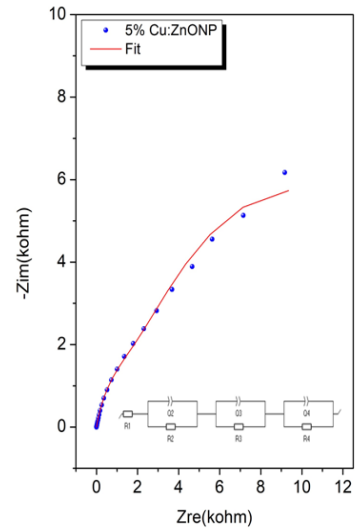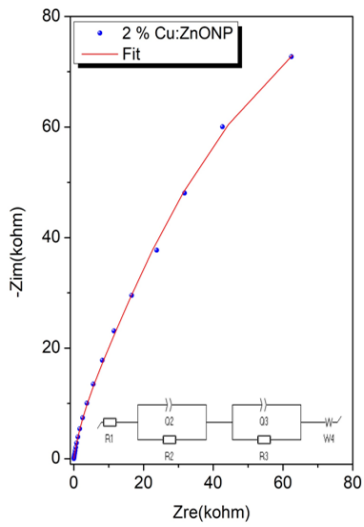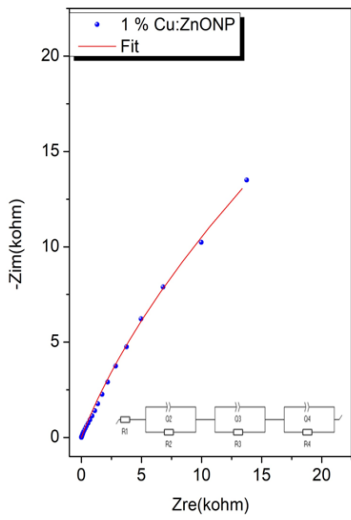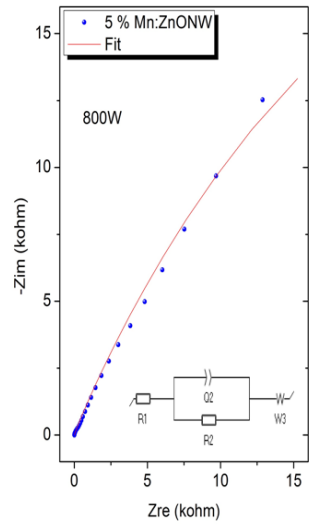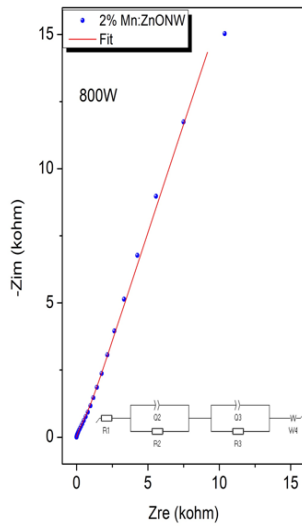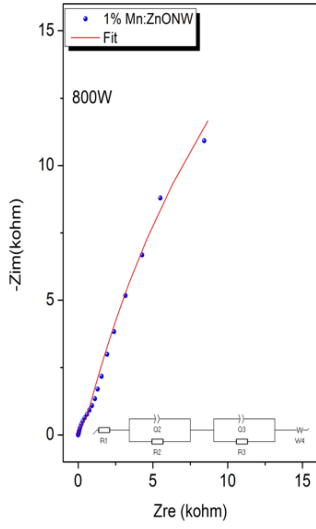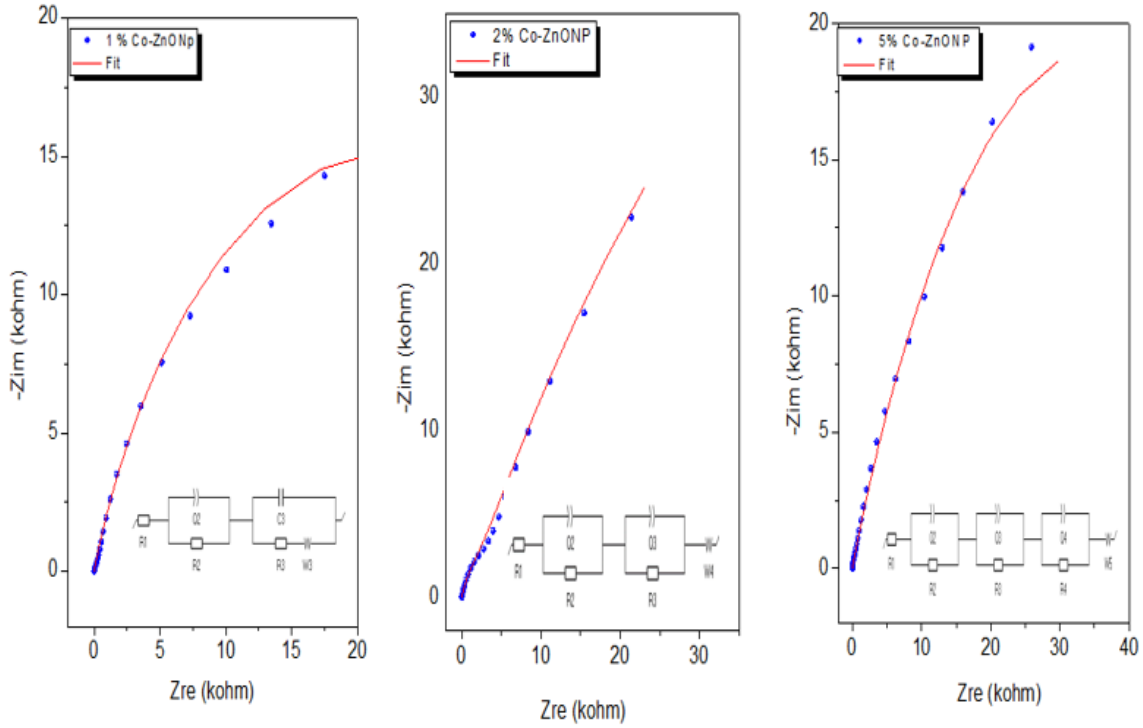
Figure 33: Equivalent circuit used to fit the Nyquist plot experimental data.

Table 11: Equivalent resistance value (Rs) of the assembled supercapacitor

	Rs (Ω)
1% Mn-doped ZnO NW 160 W	0.923
1% Mn-doped ZnO NW 800 W	0.7212
1% Cu-doped ZnO NP	1.546
1% Co-doped ZnO NP	0.925
2% Mn-doped ZnONW 160 W	0.3204
2% Mn-doped ZnONW 800 W	0.220
2% Cu-doped ZnONP	0.458
2 % Co-doped ZnO NP	0.4603

5% Mn-doped ZnO NW 160 W	0.533
5% Mn-doped ZnO NW 800 W	0.452
5% Cu-doped ZnO NP	1.093
5% Co-doped ZnO NP	2.122
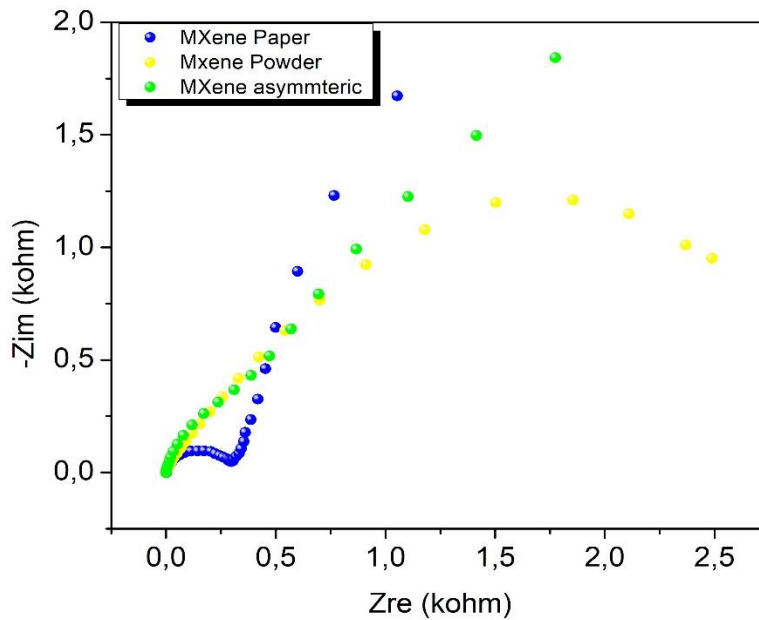
Figure 34: Nyquist plot for MXene-based supercapacitor.

5.7.3 Galvanostatic charge-discharge and Ragone plot

Fig. 35 shows the specific capacity versus potential graphs of all the supercapacitor designs at a current density of 0.10 A/g. 800 W Mn doped sample shows following the trend of the previous graphs the highest values of specific discharge capacities for 2% and 5% samples. In contrast, the Cu-doped samples show the highest values for the 1% sample. The nanowires morphology sample in general performs better in this result as well following the trends of other results. While the 2% Mn-doped ZnO samples showed the highest value of discharge capacity compared to any other design at any dopant concentration. Fig. 36 presents the specific capacity versus potential graph for the MXene-based supercapacitors and as previously obtained results MXene powder symmetric

design was the best performing compared to others. Fig. 37 shows the cyclic stability of all metal oxides-based designs, where capacitance retention was plotted with cycle number. The graphs show cycle stability for the 50th cycle and all the design shows excellent cyclic stability, where all the design shows capacitance retention of above 95% in all the cases.
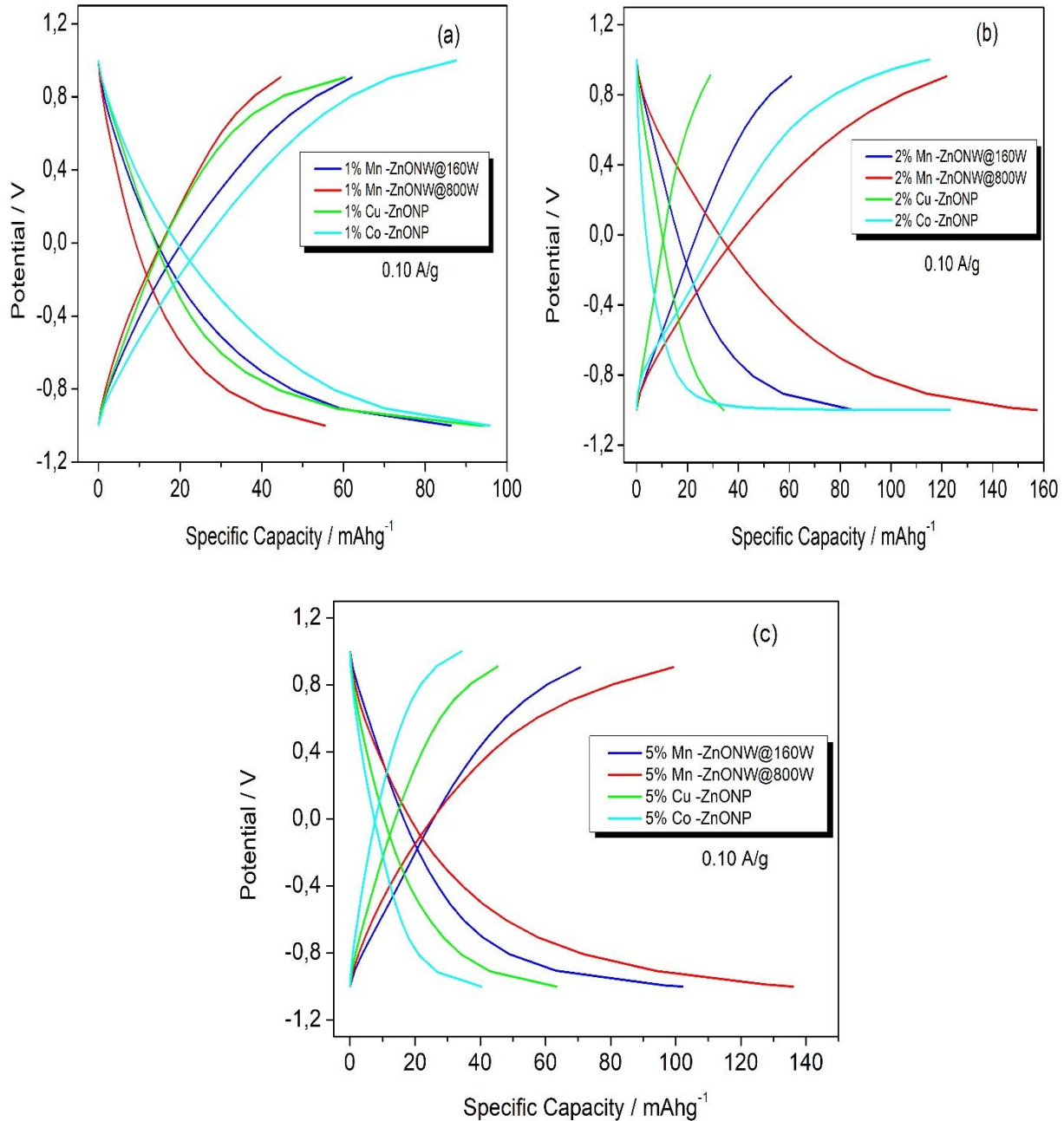
Figure 35: Galvanostatic charge-discharge curves of supercapacitor designs at 0.10 A/g current density: a) 1% doped samples, b) 2% doped samples, and c) 5% doped samples.
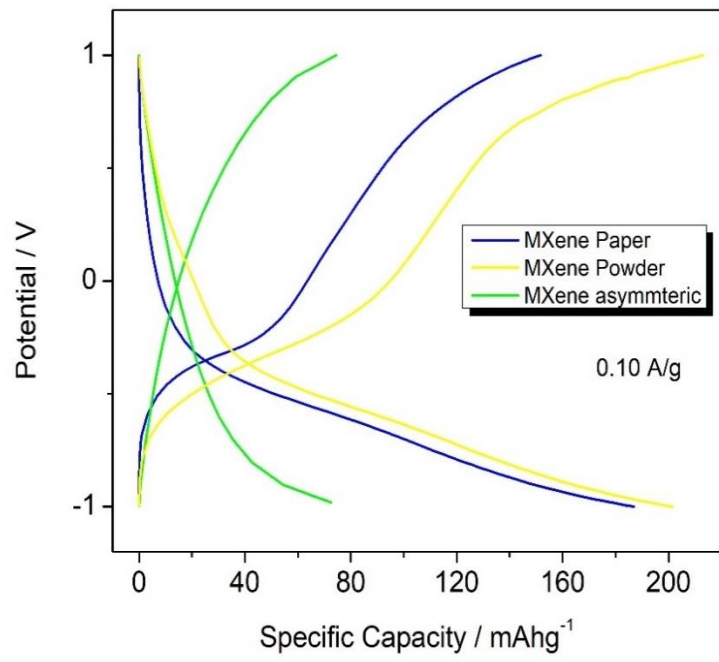
Figure 36: Galvanostatic charge-discharge curves of MXene-based supercapacitor designs.
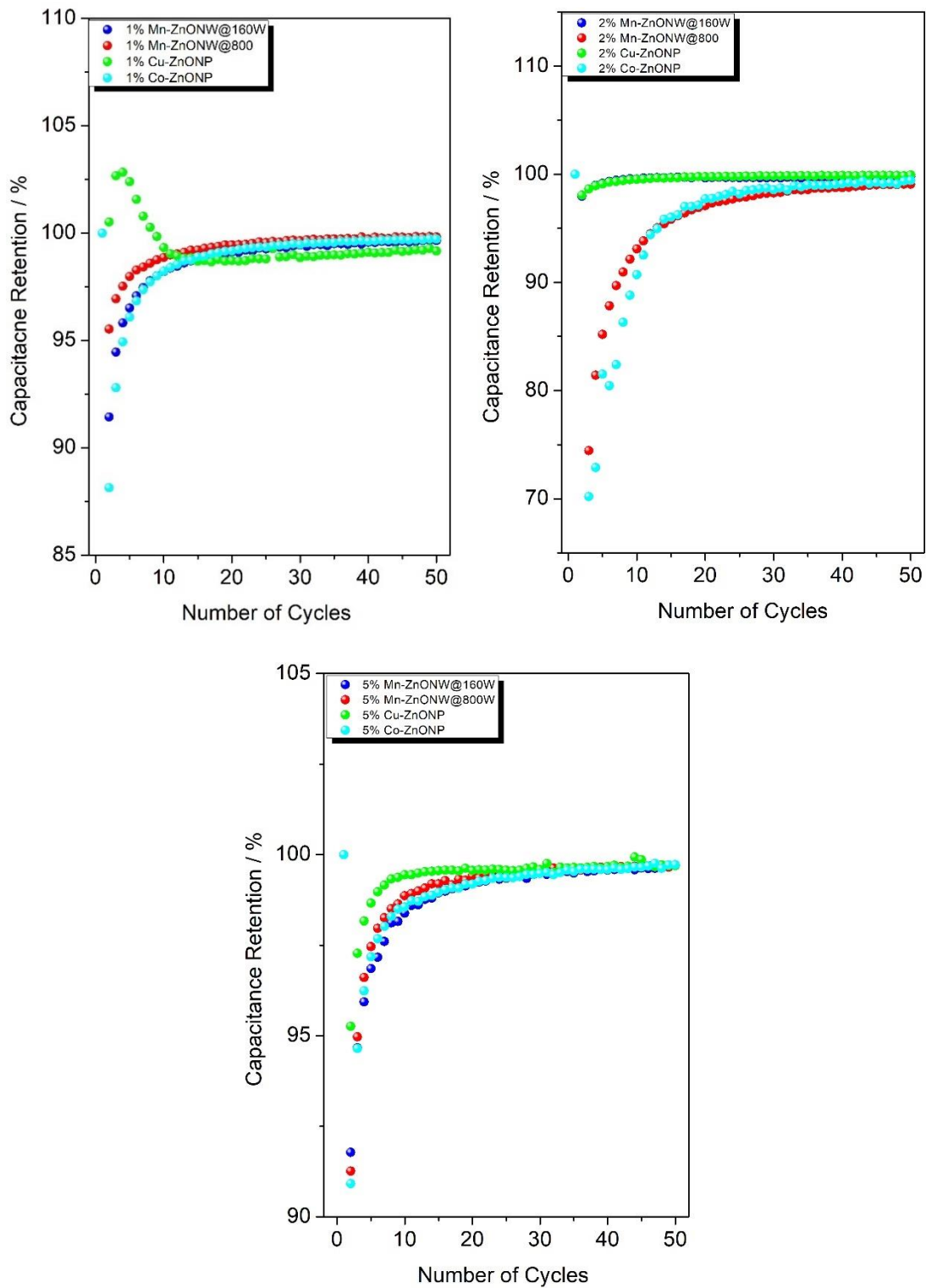
Figure 37: Capacitance retention of supercapacitor designs at a current density of 0.15 A/g

The Ragone plot is a standard performance measuring criteria for energy storage devices where the energy density and the power density values are plotted for the devices. The energy density and power density of the developed supercapacitors were measured from the galvanostatic charge-discharge data at a current density of 0.15 A/g using the following equations.

$$C = \frac{I\,\Delta t}{m\Delta V} \qquad (6)$$

$$E = 1/2\frac{C(\Delta V)^2}{3.6} \qquad (7)$$

$$P = \frac{E}{\Delta t}3600 \qquad (8)$$

Where C is the specific capacitance, I represent the current density, Δt is the time of charge and discharge cycle, ΔV is the potential window, m is the mass of the active electrode material, E is the energy density in Wh/kg and P is the power density in W/kg. Table 12 showed the obtained values of all the supercapacitor devices. Fig. 38 shows the Ragone plot for all the designs to provide the idea of where each design lies performance-wise. All values of the energy density and power density are in the region of the supercapacitor in a typical Ragone plot. However, like previous results, the 2% Mn-doped ZnO NW samples synthesized at 800 W showed the highest values of energy and power density. The overall better performance of the 2% Mn-doped sample can be attributed to firstly, its synthesis at 800 W power which gives dense nanowire morphology to provide more electrochemical sites for the reaction to take place as explained previously. While 2% doped Mn provides an optimum balance that extrinsic defect from Mn provides to the crystal structure of ZnO to enhance the supercapacitor performance without saturation and not over-straining the lattice. Zhang *et al.* showed that increasing defect centers after a certain limit will start to reduce the performance of supercapacitors [100]. Mn doping to a certain point will increase the performance and then due to excess defect sites start affecting the conductivity of the device also reported previously [101]. Where reaching the maximum performance of supercapacitor at 2% Mn doping is also reported in previous work [101-103]. Table 13 gives the specific capacitance, energy density, and power density values for the MXene-based supercapacitor, and as seen in the previous results for MXene-based devices the values of specific capacitance and energy density which are the area of interest shows very high values compare to the metal oxide-based electrode. As observed in the

previous result the MXene powder-based supercapacitors shows the highest value of specific capacitance and energy density. The result comparison from the results published in this work shows some encouraging values and provides evidence of the potential these asymmetric supercapacitor designs possess.

Table 12: Specific capacitance, energy density, and power density values obtained from galvanostatic charge-discharge at the current density of 0.15 A/g

Design	Specific Capacitance F/g	Energy density Wh/kg	Power density kW/kg
1% Mn-doped ZnO NW 160W	66.4	37	75
1% Mn-doped ZnO NW 800W	37.5	20.8	74
1% Cu-doped ZnO NP	86.6	48	75
1% Co-doped ZnO NP	79	44	74
2% Mn-doped ZnONW 160W	59	32.7	74
2% Mn-doped ZnONW 800W	151	84	75
2% Cu-doped ZnONP	24.5	5.4	3
2% Co-doped ZnO NP	102	57	75
5% Mn-doped ZnO NW 160W	78	43	73
5% Mn-doped ZnO NW 800W	86	48	75
5% Cu-doped ZnO NP	43.5	24.2	74
5% Co-doped ZnO NP	39.4	21.87	74

Table 13: MXene-based supercapacitor performance at the current density of 0.15 A/g

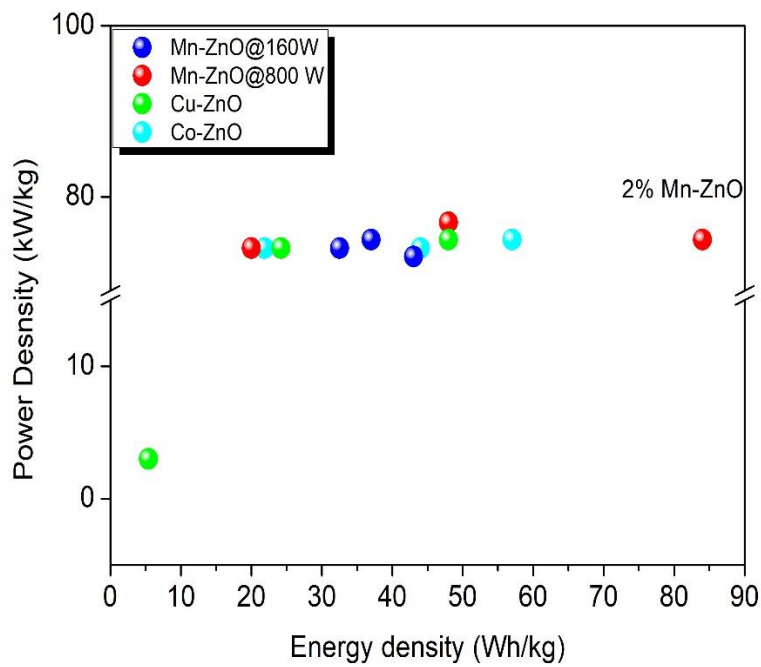| Design	Specific Capacitance F/g	Energy Density Wh/kg	Power Density kW/kg
MXene Paper	320	133	9
MXene Powder	397	176	15
MXene asymmetric	150	176	7

Figure 38: Ragone plot for metal oxide-based supercapacitor designs

6. CONCLUSIONS

In this thesis, using metal ion-doped ZnO and MXene-based electrodes are used in supercapacitors devices. Both used electrode system brings certain advantages which aid in increasing the overall performance of the supercapacitor. The synthesis of Mn, Cu, and Co-doped ZnO was provided, with proper structural and morphological analysis. The synthesized samples were used in three different doping concentrations 1%, 2%, and 5%. These samples were used in combination with MXene powder as an electrode material to assemble an asymmetric type of supercapacitor device and report the improvement in the performance of those devices with a comparative analysis for all the devices. Two types of MXene were obtained from our colleagues at Erzincan university namely MXene powder and MXene paper. The synthesis route for MXene powder and MXene paper is shown and for research purposes symmetric supercapacitor using both types of MXene as electrode material was assembled and tested. The MXene powder due to superior performance in symmetric-type supercapacitors was eventually used in combination with metal-doped samples as electrode materials. The synthesized samples were analyzed in detail by various characterization techniques to get information on structural properties by XRD, electronic properties by Raman and EPR, optical analysis by Photoluminescence spectroscopy, and electrochemical performance analysis through potentiostat. The primary importance in the analysis portion is given to the study of defect signals originating from the metal-doped ZnO as the performance of the supercapacitor depends heavily on these defects, and how we controlled these defect structures in our synthesized samples. Undoped ZnO has characteristic EPR signals that come from core and surface defects at g=1.96 and g=2.00 respectively. These defects signals were observed and after doping with metal ions the extrinsic defect that was generated by doping started to dominate intrinsic ZnO signals. EPR provided detailed information on the paramagnetic defect centers that originate when ZnO is doped with Mn, Cu, and Co, the characteristic EPR peaks were observed for all metal ions indicating successful doping and dominating extrinsic defect signals. EPR results also show how the doping concentration affects the defect structure of these samples. Photoluminescence spectroscopy on the other hand shows signals from all kinds of defects compare to EPR which only records paramagnetic defects. Photoluminescence spectroscopy results from all showed the presence of extrinsic defects which were visible in the broad signal appearing at high wavelength. The synthesized sample in combination with MXene powder was assembled in a supercapacitor

and electrochemical characterization was carried out. The analysis was performed using CV, PEIS, and GCPL, and a comparative analysis was shown. The assembled supercapacitor showed value impressive values of specific capacitance, energy density, and power density, where all design values lie within the typical supercapacitor region of the Ragone plot. In general, the nanowire morphology samples show better performance, and the 800W samples in particular show superior performance which can be attributed to the fact that these samples have a low aspect ratio which means they are denser nanowires that provide more electrochemical sites for the reaction to take place which increased the overall performance of the supercapacitors. The highest value obtained for 800 W 2% Mn-doped ZnONW shows 151 F/g specific capacitance, and 84 Wh/kg energy density at a power density of 75 kW/kg.

This research shows some valuable results but there can be also some areas where work can still be done. As discussed previously a reduction in the size will increase the surface area of the electrode material, which is an important characteristic of the electrode material. The use of ball milling in some of the design especially the one which does not perform well in comparison and then assessing their electrochemical performance can be an interesting direction where this research can be directed in the near future. Different milling times can be tested and gradual changes in the performance can be recorded to assess the impact of milling on their performance. Electrolytes which are the key component in the supercapacitor, using the same design and using them with different electrolytes like $LiPF_6$ will be a potential research window to explore and observe how it will affect the performance of our device. As different electrolytes will give a different potential window for the reaction to take place and it will lead to new results that can be compared and analyzed.

This thesis provides some encouraging results to be pursued and work further to achieve more insights into this research work. The idea of using defective structure electrodes as will help in increasing the synergy between the components of supercapacitors which will eventually increase the overall performance of the supercapacitors giving a huge window of opportunity for the researchers to work. Similar to other metal oxides, in ZnO, the defects in the materials can be tailored with different methods which again provides a potential area to work. MXene, on the other hand, has some clear advantages but it still needs some more work to make it a stable electrode. The first and most important issue that needs to be addressed is how the keep the MXene layers

delaminated as this is of constant concern among researchers of MXene that after some time it starts to stack up again. MXene used with such different electrode materials as in this work also allows making a new design with another metal ion doped ZnO and with different morphologies to make further progress in this direction.

REFERENCES

1.   Wang, X., et al., *Flexible Energy-Storage Devices: Design Consideration and Recent Progress.* Advanced Materials, 2014. **26**(28): p. 4763-4782.

2.   Guerrero, M.A., et al., *Supercapacitors: Alternative energy storage systems.* Przegląd Elektrotechniczny, 2009. **85**(10): p. 188-195.

3.   Siwal, S.S., et al., *Carbon-based polymer nanocomposite for high-performance energy storage applications.* Polymers, 2020. **12**(3): p. 505.

4.   Wayu, M., *Manganese Oxide Carbon-Based Nanocomposite in Energy Storage Applications.* Solids, 2021. **2**(2): p. 232-248.

5.   Burke, A., *Ultracapacitors: why, how, and where is the technology.* Journal of Power Sources, 2000. **91**(1): p. 37-50.

6.   Zhi, M., et al., *Nanostructured carbon–metal oxide composite electrodes for supercapacitors: a review.* Nanoscale, 2013. **5**(1): p. 72-88.

7.   Wu, Y. and C. Cao, *The way to improve the energy density of supercapacitors: Progress and perspective.* Science China Materials, 2018. **61**(12): p. 1517-1526.

8.   Wang, L., et al., *Preparation of Fe 3 O 4 with high specific surface area and improved capacitance as a supercapacitor.* Nanoscale, 2013. **5**(9): p. 3793-3799.

9.   Simon, P. and Y. Gogotsi, *Materials for electrochemical capacitors.* Nat Mater, 2008. **7**(11): p. 845-54.

10.   Chen, L.F., et al., *Synthesis of nitrogen-doped porous carbon nanofibers as an efficient electrode material for supercapacitors.* ACS Nano, 2012. **6**(8): p. 7092-102.

11.   Lin, T., et al., *Nitrogen-doped mesoporous carbon of extraordinary capacitance for electrochemical energy storage.* Science, 2015. **350**(6267): p. 1508-13.

12.   Hou, J., et al., *Tunable porous structure of carbon nanosheets derived from puffed rice for high energy density supercapacitors.* Journal of Power Sources, 2017. **371**: p. 148-155.

13.   Hou, J., et al., *Popcorn-Derived Porous Carbon Flakes with an Ultrahigh Specific Surface Area for Superior Performance Supercapacitors.* ACS applied materials & interfaces, 2017. **9**(36): p. 30626-30634.

14.   Boruah, B.D. and A. Misra, *Internal Asymmetric Tandem Supercapacitor for High Working Voltage along with Superior Rate Performance.* ACS Energy Letters, 2017. **2**(8): p. 1720-1728.

15.   Hu, C.-C., et al., *Design and tailoring of the nanotubular arrayed architecture of hydrous RuO2 for next generation supercapacitors.* Nano letters, 2006. **6**(12): p. 2690-2695.

16.   Meher, S.K. and G.R. Rao, *Ultralayered Co3O4 for high-performance supercapacitor applications.* The Journal of Physical Chemistry C, 2011. **115**(31): p. 15646-15654.

17.   Chen, S., et al., *Graphene oxide– MnO2 nanocomposites for supercapacitors.* ACS nano, 2010. **4**(5): p. 2822-2830.

18.   Zhang, X., et al., *Synthesis of porous NiO nanocrystals with controllable surface area and their application as supercapacitor electrodes.* Nano Research, 2010. **3**(9): p. 643-652.

19.   Kasap, S., et al., *Superbat: battery-like supercapacitor utilized by graphene foam and zinc oxide (ZnO) electrodes induced by structural defects.* Nanoscale Advances, 2019. **1**(7): p. 2586-2597.

20.   Genc, R., et al., *High-capacitance hybrid supercapacitor based on multi-colored fluorescent carbon-dots.* Scientific reports, 2017. **7**(1): p. 1-13.

21.   Pant, B., et al., *Carbon nanofibers wrapped with zinc oxide nano-flakes as promising electrode material for supercapacitors.* Journal of Colloid and Interface Science, 2018. **522**: p. 40-47.

22.   Song, D., et al., *Free-standing Two-dimensional Mesoporous ZnCo2O4 Thin Sheets Consisting of 3D Ultrathin Nanoflake Array Frameworks for High Performance Asymmetric Supercapacitor.* Electrochimica Acta, 2017. **257**: p. 455-464.

23.   *ZnO*. Wikipedia: Wikipedia

24.   Dubal, D.P., et al., *Ultrathin Mesoporous RuCo2O4 Nanoflakes: An Advanced Electrode for High-Performance Asymmetric Supercapacitors.* ChemSusChem, 2017. **10**(8): p. 1771-1782.

25.   Kim, C.H. and B.-H. Kim, *Zinc oxide/activated carbon nanofiber composites for high-performance supercapacitor electrodes.* Journal of Power Sources, 2015. **274**: p. 512-520.

26.   Lee, K.S., C.W. Park, and J.-D. Kim, *Synthesis of ZnO/activated carbon with high surface area for supercapacitor electrodes.* Colloids and Surfaces A: Physicochemical and Engineering Aspects, 2018. **555**: p. 482-490.

27.   Najib, S., et al., *Tailoring morphology to control defect structures in ZnO electrodes for high-performance supercapacitor devices.* Nanoscale, 2020. **12**(30): p. 16162-16172.

28.   Saleh, N.B., et al., *Importance of doping, dopant distribution, and defects on electronic band structure alteration of metal oxide nanoparticles: Implications for reactive oxygen species.* Science of The Total Environment, 2016. **568**: p. 926-932.

29.   Li, Z., et al., *3D (Three-dimensional) sandwich-structured of ZnO (zinc oxide)/rGO (reduced graphene oxide)/ZnO for high performance supercapacitors.* Energy, 2014. **69**: p. 266-271.

30.   Kalpana, D., et al., *A novel high power symmetric ZnO/carbon aerogel composite electrode for electrochemical supercapacitor.* Electrochimica Acta, 2006. **52**(3): p. 1309-1315.

31.   Rajeswari, V., R. Jayavel, and A. Clara Dhanemozhi, *Synthesis And Characterization Of Graphene-Zinc Oxide Nanocomposite Electrode Material For Supercapacitor Applications.* Materials Today: Proceedings, 2017. **4**(2, Part A): p. 645-652.

32.   Ghorbani, M., M.R. Golobostanfard, and H. Abdizadeh, *Flexible freestanding sandwich type ZnO/rGO/ZnO electrode for wearable supercapacitor.* Applied Surface Science, 2017. **419**: p. 277-285.

33.   Zhang, Y., et al., *Carbon nanotube–ZnO nanocomposite electrodes for supercapacitors.* Solid State Ionics, 2009. **180**(32): p. 1525-1528.

34.   Lu, T., et al., *Electrochemical behaviors of graphene–ZnO and graphene–SnO2 composite films for supercapacitors.* Electrochimica Acta, 2010. **55**(13): p. 4170-4173.

35.   Dillip, G.R., et al., *Oxygen Vacancy-Induced Structural, Optical, and Enhanced Supercapacitive Performance of Zinc Oxide Anchored Graphitic Carbon Nanofiber Hybrid Electrodes.* ACS Applied Materials & Interfaces, 2016. **8**(7): p. 5025-5039.

36.   Lu, T., et al., *Microwave-assisted synthesis of graphene–ZnO nanocomposite for electrochemical supercapacitors.* Journal of Alloys and Compounds, 2011. **509**(18): p. 5488-5492.

37.   Saarenpää, H., et al., *Aluminum doped zinc oxide films grown by atomic layer deposition for organic photovoltaic devices.* Solar Energy Materials and Solar Cells, 2010. **94**(8): p. 1379-1383.

38.   Takada, Y., et al., *Aluminum-doped zinc oxide electrode for robust (Pb,La)(Zr,Ti)O3 capacitors: effect of oxide insulator encapsulation and oxide buffer layer.* Journal of Materials Science: Materials in Electronics, 2014. **25**(5): p. 2155-2161.

39.   Alver, Ü. and A. Tanrıverdi, *Boron doped ZnO embedded into reduced graphene oxide for electrochemical supercapacitors.* Applied Surface Science, 2016. **378**: p. 368-374.

40.   Neelakanta Reddy, I., et al., *Structural, optical, and bifunctional applications: Supercapacitor and photoelectrochemical water splitting of Ni-doped ZnO nanostructures.* Journal of Electroanalytical Chemistry, 2018. **828**: p. 124-136.

41.   Ali, A., et al., *Mo-doped ZnO nanoflakes on Ni-foam for asymmetric supercapacitor applications.* RSC advances, 2019. **9**(47): p. 27432-27438.

42.   Angelin, M.D., et al., *Electrochemical investigation of Zr-doped ZnO nanostructured electrode material for high-performance supercapacitor.* Ionics, 2020. **26**(11): p. 5757-5772.

43.   Samuel, E., et al., *Hierarchical zeolitic imidazolate framework-derived manganese-doped zinc oxide decorated carbon nanofiber electrodes for high performance flexible supercapacitors.* Chemical Engineering Journal, 2019. **371**: p. 657-665.

44.   Alver, Ü., A. Tanrıverdi, and Ö. Akgül, *Hydrothermal preparation of ZnO electrodes synthesized from different precursors for electrochemical supercapacitors.* Synthetic Metals, 2016. **211**: p. 30-34.

45.   Luo, Q., et al., *Synthesis of ZnO tetrapods for high-performance supercapacitor applications.* Materials Letters, 2017. **198**: p. 192-195.

46.   Chaudhary, M., et al., *Ternary Au/ZnO/rGO nanocomposites electrodes for high performance electrochemical storage devices.* Applied Surface Science, 2017. **420**: p. 118-128.

47.   Garg, R., A. Agarwal, and M. Agarwal, *A review on MXene for energy storage application: effect of interlayer distance.* Materials Research Express, 2020. **7**(2): p. 022001.

48.   Rakhi, R.B., et al., *Effect of Postetch Annealing Gas Composition on the Structural and Electrochemical Properties of Ti2CTx MXene Electrodes for Supercapacitor Applications.* Chemistry of Materials, 2015. **27**(15): p. 5314-5323.

49.   Xia, Q.X., et al., *High volumetric energy density annealed-MXene-nickel oxide/MXene asymmetric supercapacitor.* RSC advances, 2017. **7**(18): p. 11000-11011.

50.   Naguib, M., et al., *Two-dimensional transition metal carbides.* ACS nano, 2012. **6**(2): p. 1322-1331.

51.   Ghidiu, M., et al., *Synthesis and characterization of two-dimensional Nb4C3 (MXene).* Chemical Communications, 2014. **50**(67): p. 9517-9520.

52.   Deysher, G., et al., *Synthesis of Mo4VAlC4 MAX Phase and Two-Dimensional Mo4VC4 MXene with Five Atomic Layers of Transition Metals.* ACS Nano, 2020. **14**(1): p. 204-217.

53.   Anasori, B., et al., *Two-Dimensional, Ordered, Double Transition Metals Carbides (MXenes).* ACS Nano, 2015. **9**(10): p. 9507-9516.

54.   Meshkian, R., et al., *Theoretical stability and materials synthesis of a chemically ordered MAX phase, Mo2ScAlC2, and its two-dimensional derivate Mo2ScC2 MXene.* Acta Materialia, 2017. **125**: p. 476-480.

55.   Yang, L., et al., *SnO2–Ti3C2 MXene electron transport layers for perovskite solar cells.* Journal of Materials Chemistry A, 2019.

56.   Lin, S.-Y. and X. Zhang, *Two-dimensional titanium carbide electrode with large mass loading for supercapacitor.* Journal of Power Sources, 2015. **294**: p. 354-359.

57.   Yan, P., et al., *Enhanced supercapacitive performance of delaminated two-dimensional titanium carbide/carbon nanotube composites in alkaline electrolyte.* Journal of Power Sources, 2015. **284**: p. 38-43.

58.   Dall'Agnese, Y., et al., *Capacitance of two-dimensional titanium carbide (MXene) and MXene/carbon nanotube composites in organic electrolytes.* Journal of Power Sources, 2016. **306**: p. 510-515.

59.   Fan, Z., et al., *Modified MXene/Holey Graphene Films for Advanced Supercapacitor Electrodes with Superior Energy Storage.* Advanced Science, 2018. **5**(10): p. 1800750.

60.   Huang, H., et al., *Massively manufactured paper-based all-solid-state flexible micro-supercapacitors with sprayable MXene conductive inks.* Journal of Power Sources, 2019. **415**: p. 1-7.

61.   Zhao, M.Q., et al., *Flexible MXene/carbon nanotube composite paper with high volumetric capacitance.* Advanced materials, 2015. **27**(2): p. 339-345.

62.   Bayram, V., et al., *MXene Tunable Lamellae Architectures for Supercapacitor Electrodes.* ACS Applied Energy Materials, 2020. **3**(1): p. 411-422.

63.   Xu, S., et al., *Flexible MXene–graphene electrodes with high volumetric capacitance for integrated co-cathode energy conversion/storage devices.* Journal of Materials Chemistry A, 2017. **5**(33): p. 17442-17451.

64.   Tang, H., et al., *MXene–2D layered electrode materials for energy storage.* Progress in Natural Science: Materials International, 2018. **28**(2): p. 133-147.

65.   Li, J., et al., *Achieving High Pseudocapacitance of 2D Titanium Carbide (MXene) by Cation Intercalation and Surface Modification.* Advanced Energy Materials, 2017. **7**(15): p. 1602725.

66.   Bragg, W.L., *The diffraction of short electromagnetic Waves by a Crystal.* Scientia, 1929. **23**(45): p. 153.

67.   Yüksel Price, B., et al., *Effects of MnO doping on the electronic properties of zinc oxide: 406 GHz electron paramagnetic resonance spectroscopy and Newman superposition model analysis.* Journal of Applied Physics, 2015. **118**(17): p. 175705.

68.   Toloman, D., et al., *Evidence by EPR of ferromagnetic phase in Mn-doped ZnO nanoparticles annealed at different temperatures.* Journal of Alloys and Compounds, 2013. **551**: p. 502-507.

69.   Thaweesaeng, N., et al., *Structure Properties of As-synthesized Cu-doped ZnO Nanopowder Synthesized by Co-precipitation Method.* Energy Procedia, 2013. **34**: p. 682-688.

70.   Mahmood, M., et al., *Synthesis of Ultrathin MnO2 Nanowire-Intercalated 2D-MXenes for High-Performance Hybrid Supercapacitors.* Energy & Fuels, 2021. **35**(4): p. 3469-3478.

71.   Fang, H., et al., *Enhanced visible light photocatalytic activity of CdS with alkalized Ti3C2 nano-sheets as co-catalyst for degradation of rhodamine B.* Journal of Materials Science: Materials in Electronics, 2019. **30**(16): p. 14954-14966.

72.   Tariq, A., et al., *Efficient Visible-Light Photocatalysis of 2D-MXene Nanohybrids with Gd3+- and Sn4+-Codoped Bismuth Ferrite.* ACS Omega, 2018. **3**(10): p. 13828-13836.

73.   Aleinawi, M.H., et al., *Spectroscopic Probing Of Mn-Doped ZnO Nanowires Synthesized via a Microwave-Assisted Route.* The Journal of Physical Chemistry C, 2022. **126**(8): p. 4229-4240.

74.   Ammar, A.U., et al., *Multifrequency EPR spectroscopy study of Mn, Fe, and Cu doped nanocrystalline ZnO.* Materials Research Bulletin, 2023. **160**: p. 112117.

75.   Vanaja, A. and K.S. Rao, *Effect of Co doping on structural and optical properties of zinc oxide nanoparticles synthesized by sol-gel method.* Advances in Nanoparticles, 2016. **5**(1): p. 83-89.

76.   Basith, N.M., et al., *Co-Doped ZnO Nanoparticles: Structural, Morphological, Optical, Magnetic and Antibacterial Studies.* Journal of Materials Science & Technology, 2014. **30**(11): p. 1108-1117.

77.   Presser, V., et al., *First-order Raman scattering of the MAX phases: Ti2AlN, Ti2AlC0.5N0.5, Ti2AlC, (Ti0.5V0.5)2AlC, V2AlC, Ti3AlC2, and Ti3GeC2.* Journal of Raman Spectroscopy, 2012. **43**(1): p. 168-172.

78.   Iqbal, A. and N.M. Hamdan, *Investigation and Optimization of Mxene Functionalized Mesoporous Titania Films as Efficient Photoelectrodes.* Materials (Basel), 2021. **14**(21).

79.   Sarycheva, A. and Y. Gogotsi, *Raman Spectroscopy Analysis of the Structure and Surface Chemistry of Ti3C2Tx MXene.* Chemistry of Materials, 2020. **32**(8): p. 3480-3488.

80.   Spanier, J.E., et al., *Vibrational behavior of the ${M}_{n+1}A{X}_{n}$ phases from first-order Raman scattering $(M=\mathrm{Ti},\mathrm{V},\mathrm{Cr},$ $A=\mathrm{Si},$ $X=\mathrm{C},\mathrm{N})$.* Physical Review B, 2005. **71**(1): p. 012103.

81.   Wang, Y., D.C. Alsmeyer, and R.L. McCreery, *Raman spectroscopy of carbon materials: structural basis of observed spectra.* Chemistry of Materials, 1990. **2**(5): p. 557-563.

82.   Melchior, S.A., et al., *High-voltage symmetric supercapacitor based on 2D Titanium Carbide (MXene, Ti2CTx)/carbon nanosphere composites in a neutral aqueous electrolyte*. 2018.

83.   Cao, Y., et al., *Enhanced thermal properties of poly(vinylidene fluoride) composites with ultrathin nanosheets of MXene.* RSC Advances, 2017. **7**(33): p. 20494-20501.

84.   Wilhelmsson, O., et al., *Deposition and characterization of ternary thin films within the Ti–Al–C system by DC magnetron sputtering.* Journal of Crystal Growth, 2006. **291**(1): p. 290-300.

85.   Myhra, S., J.A.A. Crossley, and M.W. Barsoum, *Crystal-chemistry of the Ti3AlC2 and Ti4AlN3 layered carbide/nitride phases—characterization by XPS.* Journal of Physics and Chemistry of Solids, 2001. **62**(4): p. 811-817.

86.   Mashtalir, O., et al., *Intercalation and delamination of layered carbides and carbonitrides.* Nature Communications, 2013. **4**(1): p. 1716.

87.   Jakes, P. and E. Erdem, *Finite size effects in ZnO nanoparticles: An electron paramagnetic resonance (EPR) analysis.* physica status solidi (RRL)–Rapid Research Letters, 2011. **5**(2): p. 56-58.

88.   Kaftelen, H., et al., *EPR and photoluminescence spectroscopy studies on the defect structure of ZnO nanocrystals.* Physical Review B, 2012. **86**(1): p. 014113.

89.   Ruf, T., et al., *Competing effects between intrinsic and extrinsic defects in pure and Mn-doped ZnO nanocrystals.* Journal of Nanoparticle Research, 2016. **18**(5): p. 109.

90. Ankiewicz, A., et al., *Electron paramagnetic resonance in transition metal-doped ZnO nanowires.* Journal of applied physics, 2007. **101**(2): p. 024324.

91. Savoyant, A., et al., *Core-defect reduction in ZnO nanorods by cobalt incorporation.* Nanotechnology, 2017. **28**(28): p. 285705.

92. Savoyant, A., et al., *EPR investigation of pure and Co-doped ZnO oriented nanocrystals.* Nanotechnology, 2017. **28**(3): p. 035705.

93. Misra, S.K., et al., *An X-band Co2+ EPR study of Zn1−xCoxO (x=0.005–0.1) nanoparticles prepared by chemical hydrolysis methods using diethylene glycol and denaturated alcohol at 5K.* Journal of Magnetism and Magnetic Materials, 2015. **394**: p. 138-142.

94. Nadupalli, S., et al., *About defect phenomena in ZnO nanocrystals.* Nanoscale, 2021. **13**(20): p. 9160-9171.

95. Erdem, E., *Microwave power, temperature, atmospheric and light dependence of intrinsic defects in ZnO nanoparticles: A study of electron paramagnetic resonance (EPR) spectroscopy.* Journal of alloys and compounds, 2014. **605**: p. 34-44.

96. Li, X., et al., *Carbon and Graphene Quantum Dots for Optoelectronic and Energy Devices: A Review.* Advanced Functional Materials, 2015. **25**(31): p. 4929-4947.

97. Hong, L., R.F. Klie, and S. Öğüt, *First-principles study of size- and edge-dependent properties of MXene nanoribbons.* Physical Review B, 2016. **93**(11): p. 115412.

98. Al-Asadi, A.S., et al., *Aligned carbon nanotube/zinc oxide nanowire hybrids as high performance electrodes for supercapacitor applications.* Journal of Applied Physics, 2017. **121**(12): p. 124303.

99. Yang, Q., et al., *Rationally designed hierarchical MnO2-shell/ZnO-nanowire/carbon-fabric for high-performance supercapacitor electrodes.* Journal of Power Sources, 2014. **272**: p. 654-660.

100. Zhang, J., et al., *Remarkable supercapacitive performance of TiO2 nanotube arrays by introduction of oxygen vacancies.* Chemical Engineering Journal, 2017. **313**: p. 1071-1081.

101. Prashad Ojha, D., M. Babu Poudel, and H. Joo Kim, *Investigation of electrochemical performance of a high surface area mesoporous Mn doped TiO2 nanoparticle for a supercapacitor.* Materials Letters, 2020. **264**: p. 127363.

102. Patil, D., et al., *An Mn doped polyaniline electrode for electrochemical supercapacitor.* Journal of the Electrochemical Society, 2011. **158**(6): p. A653.

103. Phonsuksawang, P., et al., *Enhancing performance of NiCo2S4/Ni3S2 supercapacitor electrode by Mn doping.* Electrochimica Acta, 2021. **368**: p. 137634.